1 **Aggregation of Slightly Buoyant Microplastics in Three-Dimensional Vortex Flows**

2 Irina I. Rypina[1], Larry J. Pratt[1], and Michael Dotzel[1]

3 [1] Woods Hole Oceanographic Institution, Physical Oceanography Department, 266 Woods Hole

4 Rd., Woods Hole, MA 02543

5 Corresponding author email: irypina@whoi.edu

Abstract

Although the movement and aggregation of microplastics at the ocean surface has been well studied, less is known about the subsurface. Within the Maxey-Riley framework governing the movement of small rigid spheres with high drag in fluid, aggregation of buoyant particles is encouraged in vorticity-dominated regions. We explore this process in an idealized model that is qualitatively reminiscent of a three-dimensional eddy with an azimuthal and overturning circulation. In the axially symmetric state, buoyant spherical particles that do not accumulate at the top boundary are attracted to a loop consisting of periodic orbits. Such a loop exists when drag on the particle is sufficiently strong. For small slightly-buoyant particles, this loop is located close to the periodic fluid parcel trajectory. If the symmetric flow is perturbed by a symmetry-breaking disturbance, additional attractors for small rigid slightly-buoyant particles may arise near periodic orbits of fluid parcels within the resonance zones created by the disturbance. Disturbances with periodic or quasi-periodic time dependence may produce even more attractors, with a shape and location that recurs periodically. However, not all such loops attract, and rigid particles released in the vicinity of one loop may instead be attracted to a nearby attractor. Examples are presented along with mappings of the respective basins of attraction.

Significance statement

This paper investigates aggregation of small, spherical, slightly buoyant, rigid particles in a simple three-dimensional vortex flow. Our goal was to gain insights into the behaviour of slightly buoyant marine microplastics in a flow that qualitatively resembles ocean eddies. Attractors are mapped out for the steady axisymmetric, steady asymmetric, and non-steady asymmetric vortices over a range of flow and particle parameters. Simple theoretical arguments are used to interpret the results.

I.   Introduction

Marine microplastic pollution has been a rising concern for the ocean environmental and for human health. Microplastics (scales < 5mm) and nanoplastics (scales < 1 μm) have been found in the tissues of marine animals, some of which are consumed by humans (Landrigan, et al. 2023). This comes at a time when global production of plastics is projected to increase. Observations of marine microplastics have been conventionally carried out using net tows and mostly occurred at or near the sea surface (van Sebille et al., 2015). However, the density of many types of microplastic particles, including high-density polyethylene, is sufficiently close to that of sea water that suspension within the water column for long periods of time is feasible. For the near-surface microplastics, Kukulka et al. (2010) and Kooi et al. (2016) present observational evidence for the fast decay in concentrations with depth over the top 5 – 20 m of the water column, with the vertical penetration of plastic particles dependent on the wind speed. Pabortsava and Lampitt (2020), on the other hand, show observational evidence for much deeper, below-the-mixed-layer subsurface peaks for three common types of microplastics in the Atlantic Ocean. Processes such as biofouling and bio-geo-chemical or photo degradation might increase the density of the plastic particles and eventually lead to the sinking of microplastics from the surface into the deeper part of the water column (Kaiser et al., 2017; Kreczak et al., 2021; Kvale et al., 2020). Consumption by biomass with the subsequent downward vertical transport is another vehicle for redistributing microplastics from the surface down. For example, Choy et al. (2019) suggest that this mechanism, specifically, consumption by pelagic red crabs and giant larvaceans, was responsible for the subsurface peaks in plastic particles concentrations observed at depths near 250 m in Monterey Bay. Thus, microplastics have been found well beneath the

80   ocean surface, but less is known regarding their spatio-temporal and size/density distributions

81   (Shamskhany et al., 2021).

82   A potentially important aspect of the movement of plastics and microplastics is aggregation, a

83   process that occurs at the surface over large scales near the centers of the five major subtropical

84   gyres and has been attributed to Ekman drift, windage and inertia (Beron-Vera, 2021). Many

85   early models concentrated on the ocean surface, but Wichmann et al. (2019) has highlighted the

86   importance of resolving the full three dimensional circulation. If aggregation also occurs below

87   the surface, well beneath the direct influence of Ekman layers, the dynamics is likely to be

88   different. Indeed, modeling results by Wichmann et al. (2019), based on a framework created by

89   Lange and van Sebille (2017) and Delandmeter and van Sebille (2019), suggests that the large

90   scale accumulation associated with the garbage patches disappears below 60m depth.

91   To avoid confusion, we will refer to infinitesimal fluid elements as "fluid parcels", and to rigid

92   plastic particles of finite size as "rigid particles". Typically the position $x_p(t)$ of a rigid particle

93   is tracked according to

94
$$x_p(t + \Delta t) = x_p(t) + \int_t^{t+\Delta t} u dt + dx_b,$$

95   where u is the fluid velocity and dx_b is an extra displacement due the non-fluid nature of the rigid

96   particle. The user can introduce custom schemes for calculating contributions to dx_b due to

97   factors such as windage and inertia (e.g. Beron-Vera et al., 2016), turbulent diffusion (e.g.

98   Kulkulka, 2012), wave induced Stokes drift (Onink et al., 2019), etc. Eulerian schemes in which

99   plastic particles are treated as concentrations, are rare, but Mountford and Morales Maqueda

100 (2019) developed an Eulerian model in which concentrations are advected by the fluid and are

101 subject to parameterized turbulence as well as sinking or rising according to a simple law

102   involving buoyancy and friction. In a similar fashion, Kvale et al. (2020) propose an Eulerian

103   model for the biological uptake and the resulting re-distribution of microplastics.

104   An alternative approach would be to use the Maxey-Riley equation (discussed below) to solve

105   for the rigid particle velocity, v, and then use the latter to compute the trajectory of that rigid

106   particle, i.e., $x_p(t + \Delta t) = x_p(t) + \int_t^{t+\Delta t} v dt$. This equation would account for the non-fluid-

107   following effects in a deductive way, however the resulting 6th-order system (for the three

108   components of velocity and position) would be computationally challenging. To better

109   understand the implications of the use of this approach while avoiding the computational burden

110   and complexity, we have elected to analyze the movement and aggregation of individual rigid

111   particles using a Maxey-Riley framework in connection with an idealized, analytically-

112   prescribed, 3D vortex flow that qualitatively resembles the geometry of the circulation in an

113   ocean eddy but is not a solution to any dynamical oceanographic equations of motion. As shown

114   by Pratt (2014) and Rypina et al. (2015), kinematic models that reproduce the correct geometry

115   are able to also reproduce the important Lagrangian features of the flow. Even in our simple

116   flow, aggregation is non-trivial, often with multiple attractors present and lack of attraction in

117   some circumstances. Thus, we wanted to thoroughly explore this simple example before

118   investigating more realistic oceanic flows. We note that other idealized studies have been carried

119   out in connection with 2D wave fields and vortex flows (e.g. DiBenedetto 2018a,b and Kelly et

120   al., 2021).

121   Aggregation can be attributed to the presence of an attractor: here, an object with a dimension

122   less than three that is somehow set up by the fluid circulation patterns and towards which rigid

123   particle trajectories attract. As long as the fluid is incompressible, fluid parcels will not

124   experience attraction and will not aggregate, but plastic particles with inertia, added mass, and

~~drag~~ may do so. Note also that because each attractor is generally associated with its corresponding basin of attraction, if rigid particles are introduced outside of the basin of attraction, they will not be attracted and will not aggregate towards this attractor.

In order to reach a better understanding of what leads to attraction and attractors in 3D flows, we explore a simple canonical example in geophysical fluid dynamics, namely the flow in a rotating cylinder. This flow resembles some of the characteristics of ocean eddies, including a horizontal swirl and an overturning component in the vertical, but is much less complex than any realistic oceanic eddy. Specifically, we use a simple analytically-prescribed phenomenological velocity introduced by Rypina et al. 2015. The Lagrangian properties of this circulation have been previously studied (Fountain, et al. 2000; Pratt et al. 2014; Rypina et al. 2015) allowing us to begin to investigate inertial rigid particles from an established base of knowledge. A prior theory (Haller and Sapsis, 2008) governing the movement of rigid particles with high drag indicates that accumulation is favored for slightly buoyant particles in flows dominated by vorticity, and this also motivates our choice of background flow. Identification of the attractors that can arise in this flow field, evaluating their reach and domains of attraction, and clarifying the circumstances that lead to their formation are the primary objectives of this work. Although motivated by the problem of marine microplastics, this study is, for now, mainly a curiosity-driven research aiming to develop a basic understanding of the mechanisms that might lead to aggregation of rigid particles in 3D flows. The hope is that with such basic understanding in hand, one could later start investigating aggregation phenomena in more complex and more realistic ocean mesoscale and submesoscale eddying flows.

II.   Methods

147 The physics of the motion of a small, rigid sphere that moves with velocity $\vec{v}(t)$ through a fluid

148 with pre-existing velocity distribution $\vec{u}(\vec{x}, t)$ has been the subject of investigation by Stokes

149 (1851), Basset (1888), Boussinesq (1903), Faxen (1922), Oseen (1927), Tchen (1947) and many

150 others, and was put in a unifying framework by Maxey and Riley (1983). More recent

151 theoretical extensions include Beron-Vera et al. (2019) and Beron-Vera (2021). We will use a

152 form of the Maxey-Riley equation that has been extended to include constant frame rotation with

153 angular velocity $\vec{\Omega}^*$:

154
$$\frac{d\vec{v}}{dt} = \frac{\rho_f}{\rho_p}\frac{D\vec{u}}{Dt} + \frac{\rho_f}{2\rho_p}\left(\frac{D\vec{u}}{Dt} - \frac{d\vec{v}}{dt}\right) - \frac{9\nu\rho_f}{2\rho_p d^2}(\vec{v} - \vec{u}) + \left(1 - \frac{\rho_f}{\rho_p}\right)\vec{g} + \frac{\rho_f}{\rho_p}\vec{\Omega}^* \times (\vec{u} - \vec{v})$$

155
$$+\frac{\rho_f}{\rho_p}2\vec{\Omega}^* \times \vec{u} - 2\vec{\Omega}^* \times \vec{v} + \left(\frac{\rho_f}{\rho_p} - 1\right)\vec{\Omega}^* \times \vec{\Omega}^* \times \vec{x}. \qquad (1)$$

156 The frame rotation was introduced into the non-rotating Maxey-Riley equation by replacing

157
$$\vec{v_s} = \vec{v_r} + \vec{\Omega} \times \vec{x_r}, \ \vec{u_s} = \vec{u_r} + \vec{\Omega} \times \vec{x_r},$$

158
$$\frac{D_s\vec{u_s}}{Dt} = \frac{D_r\vec{u_r}}{Dt} + 2\vec{\Omega} \times \vec{u_r} + \vec{\Omega} \times \vec{\Omega} \times \vec{x_r}, \ \frac{d_s\vec{v_s}}{Dt} = \frac{d_r\vec{v_r}}{Dt} + 2\vec{\Omega} \times \vec{v_r} + \vec{\Omega} \times \vec{\Omega} \times \vec{x_r},$$

159 where subscript "s" denotes stationary frame and subscript "r" – rotating frame. Alternatively,

160 transformation into a rotating frame can be done following the variational method of Ripa

161 (1987). The subscripts "r" have then been dropped in Eq. (1) and all subsequent equations since

162 all variables are now in the rotating frame. For non-spherical rigid particles, adjustments to the

163 coefficients within the Maxey-Riley equations can be made to account for elliptical shapes (see,

164 for example, DiBenedetto et al, 2018a,b and references therein) but at the cost of adding a third

165 vector equation for the orientation of the ellipsoid. However, real microplastics often have

166 complex tangled-filament-like shapes which are poorly represented by an ellipsoid, and no

167 corrections for tangled filaments are currently available.

168 In Eq. (1), which is a statement of Newton's second law for the rigid particle, the right-hand side

169 represents, in order, the effects of inertia, added mass, drag, buoyancy, Coriolis acceleration

170 associated with the added mass, the Coriolis acceleration associated with the particle mass,

171 Coriolis acceleration associated with the fluid motion, and centrifugal acceleration. A similar

172 equation has been previously derived by Beron-Vera et al. (2019), though the centrifugal

173 acceleration does not appear there explicitly, having been combined with the acceleration due to

174 gravity in order to define an effective gravity and corresponding geopotential. Coordinates are

175 then imagined to be aligned with geopotential surfaces, though standard spherical or Cartesian

176 coordinates are usually used in practice (Vallis, 2006). Our explicit retention of the centrifugal

177 acceleration will later allow absolute vorticity to arise naturally as a quantity of central

178 importance. We have omitted the lift force, the Basset history force, and the Faxen corrections

179 (Gatignol, 1983). Faxen corrections account for the variation of the flow across the rigid particle

180 and are proportional to $a^2 \Delta u$. For a particle size that is much smaller than the typical length scale

181 of the flow, these corrections are small and typically neglected (Haller and Sapsis, 2008; Beron-

182 Vera et al., 2019). The history term, which is an integral along a particle path, accounts for the

183 boundary layer effects that a particle leaves behind. It is typically ignored under the assumption

184 that the chances of other particles crossing that localized boundary layer before it decays are

185 small (Beron-Vera et al., 2019; see also Langlois et al., 2015 and Daitche and Tel., 2011 for

186 more info on the influence of the history term on the behavior of rigid particles). Finally, the lift

187 force arises when a particle rotates in a horizontally sheared flow. As shown in Beron-Vera

188 2019, the inclusion of the lift force leads to the next-order, $O(\tilde{\epsilon}^2)$ correction in the slow-

189 manifold approximation, and thus can also be neglected for small $\tilde{\epsilon}$. In Eq. (1), ρ_p and ρ_f are

190 densities of the rigid particle and the fluid, d is the particle radius, ν is viscosity of the fluid, $\vec{g}$ is

191 the gravity vector, and $\frac{D\vec{u}}{Dt} = \frac{\partial \vec{u}}{\partial t} + \vec{u} \cdot \nabla \vec{u}$ is the fluid material derivative, evaluated for

192 undisturbed fluid velocity at the position of the center of the rigid particle. The position $x(t)$ of a

193 particle is determined by

$$\frac{d\vec{x}}{dt} = \vec{v}(\vec{x}, t), \tag{2}$$

195 and together Eqs. (1) and (2) compose a coupled, 6th-order system for computation of the particle

196 position and velocity as functions of time.

197 If the velocities and lengths are nondimensionalized using characteristic scales U and L for the

198 background fluid flow, and L/U is used as a time scale, then Eq. (2) remains formally unchanged

199 while the nondimensional form of Eq. (1) is

$$\frac{d\vec{v}}{dt} = \frac{3R}{2}\frac{D\vec{u}}{Dt} + \tilde{\varepsilon}^{-1}(\vec{v} - \vec{u}) + \left(1 - \frac{3R}{2}\right)\vec{g}_r + 3R\vec{\Omega} \times (\vec{u} - \vec{v}) + 2\left(\frac{3R}{2} - 1\right)\vec{\Omega} \times \vec{v}, \tag{3}$$

201 where $= \frac{2\rho_f}{\rho_f + 2\rho_p}$, $\vec{g}_r = (\vec{g} - \vec{\Omega}^* \times \vec{\Omega}^* \times \vec{x})/(\frac{U^2}{L})$, $\vec{\Omega} = \frac{\vec{\Omega}^* L}{U}$ and $\tilde{\varepsilon} = \frac{2}{9}\left(\frac{d}{L}\right)^2 \frac{UL}{\nu}\frac{1}{R}$ is the Stokes

202 number, the ratio of the adjustment time scale of a particle (due to drag) to the time scale of the

203 background flow. For $\tilde{\varepsilon} \ll 1$, viscous drag is the dominant force acting on the particle, implying

204 that a particle with an initial velocity differing by an amount $> O(\tilde{\varepsilon})$ from the local fluid velocity

205 will be rapidly accelerated over a time scale $\tilde{\varepsilon}$ to a velocity proximal to that of the fluid.

206 Thereafter the particle will undergo a slow evolution in which the weaker forces due to inertia,

207 added mass, and buoyancy cause slight departures from the movement of the fluid itself.

208   The limit $\tilde{\varepsilon} \to 0$ constitutes a singular perturbation of Eq. (3), a problem that can be addressed

209   using an approach due to Fenichel (1979) that was originally formally developed for a steady

210   background flow, but that has been extended by Haller and Sapsis (2008) to include a time-

211   varying background flow. In either case, it can be shown that following the initial viscous

212   adjustment, the particle position and velocity tend toward a subspace or "slow manifold" on

213   which the particle velocity is determined directly by the fluid velocity through an "inertial"

214   equation, here extended to include frame rotation:

215    $$\vec{v} = \vec{u} + \tilde{\varepsilon} \ \left(\frac{3R}{2} - 1\right)\left[\frac{D\vec{u}}{Dt} + 2\vec{\Omega} \times \vec{u} - \vec{g}_r\right] + O(\tilde{\varepsilon}^{\,2}). \tag{4}$$

216   This result is the same as obtained by Beron-Vera et al. 2019, provided that their gravity vector

217   is interpreted as our $\vec{g}_r$. The same authors also present more general cases, including those with

218   the lift force and on the sphere. In Supplementary Material we present a simple derivation of Eq.

219   (4) based on a multiple-scale expansion. It provides a quick, though less rigorous, alternative to

220   the Fenichel approach.

221   A chief advantage of the slow manifold reduction is that the 6th order system given by Eqs. (2)

222   and (3), in which particle velocity needs to be solved for, is reduced to a 3rd order system given

223   by Eqs. (2) and (4), where the particle velocity is explicitly written as a function of fluid velocity

224   and flow and particle parameters (and thus is known). The bracketed expression in Eq. (4), which

225   determines the velocity of the rigid particle relative to the fluid, is nothing more than $\frac{\partial}{\partial x_j}\tau_{ij}$,

226   where τ_{ij} is the stress tensor for the fluid. Thus the relative velocity of a rigid particle on the

227   slow manifold is in the same direction as the net force that would act on a fluid parcel occupying

228   the same space. Ordinarily, for a fluid parcel, that force would equate with an acceleration, but

229   on the slow time scale, the relative particle velocity points in the same direction as the net fluid

230   force and its magnitude is proportional to $\tilde{\varepsilon}\left(\frac{3R}{2} - 1\right) = \frac{2}{9}\frac{d^2}{L^2}\frac{UL}{\nu}\frac{(\rho_f - \rho_p)}{\rho_f}$. Since the aggregation of

231   rigid particles requires departures of the particle velocity from the (divergence free) velocity

232   field of the fluid, one can expect that aggregation will occur more slowly if d and $(\rho_f - \rho_p)/\rho_f$

233   are small, or if ν is large. At the same time, the existence of attractors internal to the fluid may

234   depend on $(\rho_f - \rho_p)/\rho_f$ being small: for example, a large density difference may mean that

235   rigid particles simply sink to the bottom or rise to the surface (and are thus attracted to attractors

236   external to the fluid interior).

237   As pointed out by Haller and Sapsis (2008) (also see Beron-Vera et al. 2019), we can consider a

238   continuous concentration of rigid particles with similar properties, and with smoothly varying

239   velocity given by Eq. (4). The aggregation of such a concentration would appear to require that

240   the divergence of that velocity be negative (though see an apparent counterexample in Fig 1c,

241   presented later). Following Haller and Sapsis (2008), consider the evolution of a material

242   volume of rigid particles. The time rate of change of this volume is

243    $\frac{dV}{dt} = \oiint \vec{v} \cdot \vec{n}\, dA_V = \iiint (\nabla \cdot \vec{v})\mathrm{dV} = \iiint \nabla \cdot \left[\vec{u} + \tilde{\varepsilon}\left(\frac{3R}{2} - 1\right)\left(\frac{D\vec{u}}{Dt} + 2\vec{\Omega} \times \vec{u} - \vec{g}_r\right)\right]\mathrm{dV}$ (5)

244   where $\nabla \cdot \vec{u} = 0$ for an incompressible fluid. Shrinking V to an infinitesimal size allows the right-

245   hand side to be approximated by V times the local value in the integrand, and the result may be

246   integrated in time, yielding

247    $V(t) = V_0 \exp\left(\tilde{\varepsilon}\ \left(\frac{3R}{2} - 1\right)\int_{t_0}^{t} \nabla \cdot \left(\frac{D\vec{u}}{Dt} + 2\vec{\Omega} \times \vec{u} - \vec{g}_r\right)ds\right)$

248    $= V_0 \exp\left(-2\tilde{\varepsilon}\ \left(\frac{3R}{2} - 1\right)\int_{t_0}^{t}[Q_r(x(s), s) + \vec{\Omega} \cdot \vec{\zeta}_r + \left|\vec{\Omega}\right|^2]\,ds\right)$

249
$$= V_0 exp\left(-2\tilde{\varepsilon}\ \left(\frac{3R}{2}-1\right)\int_{t_0}^{t}Q_a(x(s),s)ds\right).$$
(6)

250 Here $Q_r = \frac{1}{2}\left(\frac{1}{2}\left|\vec{\zeta}_r\right|^2 - |S|^2\right)$ is the three-dimensional Okubo-Weiss parameter (Okubo, 1970;

251 Weiss, 1991), $\vec{\zeta}_r$ represents the relative vorticity vector for the fluid, $S = 1/2(\nabla\vec{u} + (\nabla\vec{u})^T)$ is

252 the strain tensor, and $|S|$ is its Frobenius norm. The final step in Eq. (6) follows from

253 introduction of the absolute vorticity vector

254 $\vec{\zeta}_a = \vec{\zeta}_r + \overrightarrow{2\Omega}$
(7)

255 and the corresponding function $Q_a = \frac{1}{2}\left(\frac{1}{2}\left|\vec{\zeta}_a\right|^2 - |S|^2\right).$ We note that for a volume V of any

256 size:

257 $\frac{dV}{dt} = 2\tilde{\varepsilon}\ \left(\frac{3R}{2}-1\right)\iiint Q_a\,\mathrm{d}V = \tilde{\varepsilon}\ \left(\frac{3R}{2}-1\right)\iiint \frac{\partial^2}{\partial x_i \partial x_j}\tau_{ij}\,\mathrm{d}V = \frac{2}{9}\frac{d^2}{L^2}\frac{UL}{\nu}\frac{(\rho_f-\rho_p)}{\rho_f}\oiint \frac{\partial}{\partial x_j}\tau_{ij}n_i\,dA_V,$

258 (8)

259 where n_j denote the components of the outward unit vector normal to the bounding surface A_V.

260 The first equality in Eq. (8) is a modest modification of Eq. (31) from Haller and Sapsis (2008),

261 and one could probably have guessed that our more general result could be obtained by replacing

262 Q with Q_a. The remainder of the equation expresses volume changes in terms of the fluid

263 stresses. Thus for buoyant particles, a volume $V(t)$ of any size will contract if the force normal

264 to A_V due to the fluid stresses, integrated around A_V, is inward. In many cases, including

265 quasigeostrophic eddies and gyres, internal waves, and the surface gravity waves considered by

266 DiBenedetto et al. (2018a,b) and all inviscid flows, the stress tensor is dominated by pressure,

267 i.e., $\frac{\partial}{\partial x_j}\tau_{ij} \cong -\frac{1}{\rho_f}\nabla p$, so the tendency to aggregate is determined entirely by the pressure field.

268   In general, Q_a can change sign along a particle trajectory, making it hard to predict whether the

269   surrounding volume shrinks or expands with time. If a buoyant particle is trapped in a region in

270   which Q_a is predominatly positive, then this region is a good candidate for aggregation.

271   Persistent ocean eddies and other vortical structures are possibilities, not only because vorticity

272   tends to dominate over strain, but also because such features have the ability to trap fluid for long

273   periods of time. For dense particles, contraction occurs in areas dominated by strain, and it has

274   been shown that aggregation of heavy particles can occur in strain-dominated filaments that arise

275   in particle-laden turbulent flows, though the considered particle-to-fluid density differences tend

276   to be quite large (see Brandt and Coletti, 2022 for a review). In our study, we will focus on

277   vortex flows reminiscent of ocean eddies, and on lower dimension objects within such flows that

278   can act as attractors for buoyant particles.

279   A simple example of aggregation is given by Haller and Sapsis (2006), who argue that the

280   elliptical center of a steady, non-divergent 2d eddy, with $\vec{g} = |\vec{\Omega}| = 0$, acts as an attractor for

281   buoyant particles. Here Q_a (now $=Q_r$), is ostensibly positive near the elliptical center of the

282   eddy, corresponding to contraction of the phase space (which in our case coincides with the

283   physical space) of the rigid particle motion. Since the central fixed point of the velocity field of

284   the eddy is also a fixed point of the slow manifold particle velocity (Eq. (4)), buoyant particles

285   initiated about the center should migrate towards the center. If the eddy is inviscid and its

286   streamlines are circular, then the pressure and azimuthal velocity are related by the cyclostrophic

287   balance $\frac{1}{\rho_f}\frac{\partial p}{\partial r} = \frac{u_\theta^2}{r}$ so that $2Q_r = \frac{1}{\rho_f}\left(\frac{1}{r}\frac{\partial p}{\partial r} + \frac{\partial^2 p}{\partial r^2}\right)$, and for an eddy in solid body rotation ($u_\theta =$

288    $\Gamma_s r$), $2Q_r = \frac{1}{\rho_f}\left(\frac{1}{r}\frac{\partial p}{\partial r} + \frac{\partial^2 p}{\partial r^2}\right) = 2\Gamma_s^2$. As suggested in Figure 1a, a small concentration of rigid

289   particles indicated by the cross hatched area shrinks as it moves towards the center of the eddy.

290   The contraction is partially due to the geometric effect of movement towards smaller radius

291   (term $\frac{1}{r}\frac{\partial p}{\partial r}$) but also due to the fact that the pressure gradient decreases to zero as the center is

292   approached and thus the inner edge of the path moves more slowly inward than the outer part

293   (term $\frac{\partial^2 p}{\partial r^2}$). In the case of solid body rotation the two terms contribute equally. A second

294   example (Fig. 1b) is of an eddy with an azimuthal velocity given by $u_\theta = \Gamma_C r^{1/2}$. Here $\frac{\partial^2 p}{\partial r^2} = 0$

295   and $2Q_r = \frac{1}{\rho_f}\left(\frac{1}{r}\frac{\partial p}{\partial r}\right) = \Gamma_C^2/r > 0$, so the contraction of the patch is entirely due to the geometric

296   effect of its movement towards smaller radius. The most curious case is that of a point vortex:

297    $u_\theta = \Gamma_P r^{-1}$, for which $2Q_r = \frac{1}{\rho_f}\left(\frac{1}{r}\frac{\partial p}{\partial r} + \frac{\partial^2 p}{\partial r^2}\right) = \frac{\Gamma_P^2}{r^4} - \frac{3\Gamma_P^2}{r^4} < 0$. Here the vorticity is zero away from

298   the eddy center and the velocity field is dominated by strain. The pressure gradient *increases* as

299   the center of the vortex is approached, meaning that the inner part of the patch moves towards

300   the center more rapidly than the outer portion (Fig. 1c) and this tendency (quantified by the

301   factor $-\frac{3\Gamma_P^2}{r^4}$) surpasses the tendency towards geometrical contraction (quantified by the factor

302    $\frac{\Gamma_P^2}{r^4}$). The area of the patch thus expands as rigid particles are drawn towards the center of the

303   vortex. Note, however, that a patch surrounding the center of the vortex can only shrink. This

304   behavior is made possible by the singularity at the center, and although this feature is artificial,

305   point vortices are often used in idealized models of fluid flow and will act as sinks or "black

306   holes" for buoyant particles even though $2Q_r < 0$.

307   The sign of Q_a is clearly not the whole story and does not encompass the effects of boundaries.

308   For example, consider the fate of heavy ($\rho_f < \rho_p$) particles in the eddy show in Fig. 1a. The

309   particles will migrate outward in each case, and no interior attraction will occur unless the eddy

310   is surrounded by a boundary, which would then act as an attractor.

311 In the next section, we will consider a more general, 3D, eddy-like circulation: one that has both

312 vertical and horizontal components of vorticity, time dependence, and a variety of vortical

313 structures that act as candidates for attraction. Our model is based on the incompressible flow in

314 a rotating cylinder (Greenspan, 1986), which has been studied in many configurations by

315 numerous authors as a model of ocean circulation (Hart and Kittelman, 1996; Pedlosky & Spall,

316 2005), ocean eddies (Pratt et al., 2014; Rypina et all., 2015), or industrial processes and

317 engeneering applications (Lopez & Marques, 2010 and references therein), and can be easily set

318 up in the laboratory setting (Fountain et al., 2000; Lackey and Sotiropoulos (2006)). It its

319 original configuration the cylinder rotates about a vertical axis at a constant (positive) angular

320 velocity $(\vec{\Omega} = \Omega\vec{k})$, and the lid, which is in contact with the fluid, rotates with a slightly greater

321 angular speed. The differential rotation sets up an azimuthal circulation in the horizontal and an

322 overturning circulation in the vertical. (Overturning is observed in ocean eddies as well and

323 Ledwell et al. (2008) present an example.) The steady, axially symmetric state of the rotating

324 cylinder flow that is established will be our first object of investigation. A steady but

325 asymmetrically-perturbed variant can be established by moving the axis of rotation of the lid

326 away from the axis of rotation of the cylinder, and this offset can also be varied in order to

327 induce time dependence. Fountain et al. (2000) set a similar situation up in a laboratory cylinder

328 using a submerged impeller that can be tilted, rather than the differentially rotating lid that can be

329 shifted, to establish an asymmetric disturbance flow. The authors discussed the Lagrangian

330 characteristics of the undisturbed flow and demonstrated the existence of secondary vortical

331 structures generated when the flow is perturbed. Pratt et al. (2014) reproduced similar structures

332 using a primitive equation simulation and explored the rich assembly of chaotic regions and non-

333 chaotic vortical structures as functions of the Ekman and Rossby numbers of the flow. The time-

334 dependent version of the rotating cylinder flow and a theory describing the resulting vortical

335 structures were discussed by Rypina et al. (2015), who based their examples on a

336 phenomenological model that reproduced many of the qualitative features of the numerically-

337 obtained velocity field. In dimensionless Cartesian coordinates, the model velocity field is given

338 by

339 $\quad u^{(x)} = -bx(1-2z)\frac{r_o-r}{3} - ay(c+z^2) + \varepsilon\left[y(y-y_o+\gamma cos(\sigma t)) - \frac{r_o^2-r^2}{2}\right](1-\beta z),$ (9a)

340 $\quad u^{(y)} = -by(1-2z)\frac{r_o-r}{3} + ax(c+z^2) - \varepsilon x(y-y_o+\gamma cos(\sigma t))(1-\beta z),$ (9b)

341 $\quad u^{(z)} = bz(1-z)\frac{2r_o-3r}{3},$ (9c)

342 in which $r = (x^2+y^2)^{1/2}$ and r_o is the cylinder radius. The velocity field consists of a steady,

343 axially symmetric flow of strength a with an overturning circulation of strength b. To this

344 symmetric state one can add an asymmetric, possibly unsteady and depth dependent, perturbation

345 of amplitude ε (not to be confused with the Stokes number $\tilde{\varepsilon}$). The perturbation is quantified by

346 an offset parameter y_o that introduces axial asymmetry in the velocity field, a frequency σ, and

347 an amplitude β for linear depth dependence and an amplitude γ for the time dependence. For the

348 case of axially symmetric, steady flow ($\varepsilon = 0$) the horizontal velocity field, in cylindrical

349 coordinates, becomes

350 $\qquad\qquad u^{(r)} = -br(1-2z)\frac{r_o-r}{3}$ (10a)

351 and

352 $\qquad\qquad u^{(\theta)} = ar(c+z^2),$ (10b)

353   where θ is the azimuthal angle. Table 1 lists the parameter values used for each numerical

354   experiment.

355   We now review the main features of the Lagrangian circulation in the rotating cylinder flow. In

356   the steady, symmetric configuration, each fluid trajectory is confined to the surface of a torus as

357   it winds around the cylinder. The typical torus is associated with quasi-periodic trajectories and

358   any such trajectory, followed for a sufficient length of time so that it completes many

359   overturning and azimuthal rotations around the cylinder, will sketch out the torus in 3D. Fig. 2b

360   contains several examples of such tori and Fig. 2a shows the corresponding Poincare map, made

361   by marking the crossing points of trajectories through a vertical slice through the cylinder. After

362   a large number of crossings each quasi-periodic trajectory traces out the cross section of the torus

363   on which it lives. The tori are nested within each another, with a single, horizontal, periodic

364   trajectory located at the center of the nest. Certain tori contain periodic trajectories, and these

365   will show up as a finite number of dots on the Poincare map. Because of this geometry, the

366   motion of fluid parcels is most naturally described in terms of action-angle-angle variables,

367   where the action, I, acts a label for a particular torus and is constant following each trajectory,

368   and the two angle variables, $\tilde{\theta}$ and ϕ, define the location of a parcel on the torus. Here $\tilde{\theta}$ is an

369   azimuthal angle that differs from the above cylindrical coordinate θ in how its origin is defined,

370   while the 'poloidal' angle ϕ wraps around the cross-section of each torus. The coordinates are

371   non-orthogonal but are defined in such a way that the angular velocities, $\Omega_{\tilde{\theta}}$ and Ω_{ϕ}, are also

372   constant following a trajectory. The explicit transformations to the action-angle-angle variables

373   are given in Mezic and Wiggins (1994).

374   When the symmetric RC flow is perturbed by a small, steady, symmetry-breaking perturbation,

375   as controlled by the parameters ε and y_o in Eq. (9), the tori that are populated by periodic orbits

376   potentially become resonant and break up, resulting in chaotic motion of fluid parcels in the

377   vicinity (Fig. 2d-i). Tori with quasiperiodic orbits deform but stay intact. Examples are discussed

378   by Fountain et al. (2000) and Pratt et al. (2013), and the latter found that chaos generally

379   dominates in a large region that includes the central axis of the cylinder and extends around the

380   boundaries of the cylinder. Away from this region the space is occupied by tori that have

381   survived the perturbation, and these are sandwiched between tori that have broken up and created

382   braided regions of chaos. The breakup of a torus also gives rise to new tori that appear as islands

383   in the Poincare maps (Fig. 3d and 3g) and these contain non-chaotic trajectories. The number of

384   islands can be predicted by a theory that decomposes the symmetry-breaking perturbation into

385   Fourier modes, written in the $(I,\ \tilde{\theta}, \phi)$ coordinates, with wave numbers n and m in the $\tilde{\theta}$ and ϕ

386   direction. If the angular velocities $\Omega_{\tilde{\theta}}$ and Ω_{ϕ} characterizing the trajectories on a particular torus

387   satisfy the resonance condition $n\Omega_{\tilde{\theta}} + m\Omega_{\phi} = 0$ for some n and m, equivalent to the trajectories

388   on that torus being periodic, then that torus will break up and a new set of invariant tori (islands)

389   will form. Running through the center of the islands will be a periodic trajectory that will execute

390   n azimuthal cycles to every m poloidal (overturning) cycles. In the case shown in Fig. 3a,

391    $n = m = 1$, so the periodic trajectory circles the cylinder horizontally once for each overturning

392   cycle: a so-called $1:1$ resonance.

393   If the symmetry breaking perturbation is quasi-periodic in time, with underlying frequencies σ_i,

394   the resonance condition for the breakup of a torus becomes $n\Omega_{\tilde{\theta}} + m\Omega_{\phi} + l_i\sigma_i = 0$, where l_i's

395   are integers (Rypina, et al. 2015). Unlike the resonance condition for the steady perturbation,

396   which is only satisfied on tori foliated by periodic trajectories, this new resonant condition may

397   be satisfied on tori that have quasi-periodic orbits, and the resonant islands that form will have a

398   shape and location that vary in time. An example (Fig. 2g,h) of the case of a resonance with a

399   single-frequency (i.e., time-periodic) perturbation shows a number of resonant islands. These

400   features vary in time, recovering their shape and location periodically, and the snapshots shown

401   are obtained by strobing the trajectories in 3D and at the forcing frequency. The green and blue

402   islands in Fig. 2h have resulted from the breakup of tori with quasiperiodic trajectories, and

403   center of the island corresponds to a closed material curve that is populated with quasiperiodic

404   trajectories.

405   Note that the resonance condition above and our results in general are applicable to quasi-

406   periodic disturbances with finite number of frequencies, rather than only periodic disturbances.

407   (We only show numerical simulations for the time-periodic case for simplicity.) Because any

408   broad-spectrum function can be arbitrary closely represented by a quasi-periodic function with a

409   finite number of frequencies, this could be applicable to some oceanic flows, especially those

410   with pronounced peaks in the spectrum. However, for flows with truly broadband spectrum, this

411   approach is probably poorly applicable and/or at least impractical because of the very large

412   number of discrete frequencies needed. This is similar in its utility/applicability to other

413   Kolmogorov-Arnold-Moser—based and resonance—based arguments used in prior papers by

414   many authors (including both us and the reviewer), see, for example, Rypina et al., 2007 and

415   Beron et al., 2008; 2010.

416   **III.   Results**

417   Aggregation of rigid particles will occur in presence of an attractor, an object with a dimension

418   < 3 to which particles tend asymptotically in time. We are most interested in attractors that

419   occur in the interior of the rotating cylinder, and are set up by the background circulation, as

420   opposed to the physical boundaries of cylinder. We will see that a closed material contour

421   consisting of periodic orbits near the core of the nested tori in the steady symmetric case act as

422   an attractor for slightly buoyant particles, and that similar material contours consisting of

423   periodic or quasiperiodic orbits near the centers of the resonant islands in the asymmetric cases

424   can play the same role. We will explore three cases in increasing complexity, beginning with

425   steady flows with axial symmetry, and proceeding to steady, asymmetric flows and finally

426   unsteady asymmetric flows.

427   The search for attractors is motivated by the hypothesis that for cases of strong drag, where the

428   rigid particle velocity lies close to the fluid velocity, a periodic orbit for the rigid particle motion

429   will exist in the vicinity of a periodic trajectory for the fluid parcel motion, and that if $Q_a > 0$ in

430   a region surrounding the latter, that it should attract buoyant particles. For the time-dependent

431   case, we extend the search to included closed loops that contain recirculating rigid particles and

432   that vary periodically in time.

433   (a) steady, axially-symmetric 3D flows

434   The fluid velocity field for this case is given by Eqs. (9c) and (10), and these indicate that the

435   location of the horizontal, periodic fluid parcel trajectory living at the center of the nested tori, is

436   given by $r = 2r_o/3$ and $z = \frac{1}{2}$. It is natural to ask whether a periodic trajectory for rigid particles

437   also exists nearby. In the slow-manifold approximation, the steady radial, azimuthal and vertical

438   particle velocities are obtained by writing Eq. (4) in cylindrical coordinates, leading to

439
$$v^{(r)} = u^{(r)} + \tilde{\varepsilon}\left(\frac{3R}{2} - 1\right)\left[\left(u^{(r)}\frac{\partial}{\partial r} + u^{(z)}\frac{\partial}{\partial z}\right)u^{(r)} - u^{(\theta)}\left(2\Omega + \frac{u^{(\theta)}}{r}\right) - \Omega^2 r\right] \qquad (11a)$$

440 $\quad v^{(\theta)} = u^{(\theta)} + \tilde{\varepsilon}\left(\frac{3R}{2} - 1\right)\left[\left(u^{(r)}\frac{\partial}{\partial r} + u^{(z)}\frac{\partial}{\partial z}\right)u^{(\theta)} + u^{(r)}\left(2\Omega + \frac{u^{(\theta)}}{r}\right)\right]$ $\qquad$ (11b)

441 $\quad v^{(z)} = u^{(z)} + \tilde{\varepsilon}\left(\frac{3R}{2} - 1\right)\left[\left(u^{(r)}\frac{\partial}{\partial r} + u^{(z)}\frac{\partial}{\partial z}\right)u^{(z)} + g\right]$ $\qquad$ (11c)

442 *Position of attracting periodic orbit; approximate analytical expression on a slow manifold*

443 Searching for points $r = r_c$ and $z = z_c$ for which $v^{(r)} = v^{(z)} = 0$, and that lie in the proximity of

444 the horizontal trajectory of the flow, we introduce

445 $\quad r_c = \frac{2r_o}{3} + \tilde{\varepsilon}\left(\frac{3R}{2} - 1\right)\tilde{r}$ and $z_c = \frac{1}{2} + \tilde{\varepsilon}\left(\frac{3R}{2} - 1\right)\tilde{z}$.

446 Substituting into the right-hand sides of (11a,c) and setting both to zero results, after neglect of

447 $O(\tilde{\varepsilon}^2)$ terms, in

448 $\quad r_c = \frac{2r_o}{3} + \tilde{\varepsilon}\left(\frac{3R}{2} - 1\right)\frac{g}{b}r_o$ $\qquad$ (12a)

449 and

450 $\quad z_c = \frac{1}{2} + \frac{9}{2br_o}\tilde{\varepsilon}\left(\frac{3R}{2} - 1\right)\left[\Omega^2 + a\left(c + \frac{1}{4}\right)\left(2\Omega + a\left(c + \frac{1}{4}\right)\right)\right].$ $\qquad$ (12b)

451 For the parameters $a > 0$ and $b > 0$, circulation is cyclonic with upwelling in the center of the

452 cylinder, and $(3R/2) - 1 > 0$ for buoyant particles, so the $O(\tilde{\varepsilon})$ corrections are positive and the

453 periodic particle orbit lies at larger radius and elevation than the periodic fluid orbit. Note also

454 from Eq. (11b) that the azimuthal velocity component of the rigid particle on the periodic orbit is

455 equal to that of the fluid.

456 An explanatory sketch (Fig. 3) shows the position of the periodic orbit of the rigid particle

457 relative to that of the periodic orbit of the fluid. Since the rigid particle is buoyant, it can

458 maintain its level z only if it is situated in a region where the vertical fluid velocity is < 0, here

459 to the right of the fluid periodic orbit. Also, the horizontal pressure gradients associated with the

460 centripetal acceleration associated with the frame rotation (term $\Omega^2 r$), the Coriolis acceleration

461 (term $2\Omega u^{(\theta)}$), and the centripetal acceleration due to the azimuthal velocity $u^{(\theta)^2}/2r$ are all

462 positive for this flow, so that low pressure exists at $r=0$ and the rigid particle is forced

463 horizontally inward. To remain stationary the particle must sit in a region where the radial

464 velocity of the fluid is outward. In this manner, the periodic trajectory exists at a location where

465 the forces of inertia, buoyancy and added mass can be countered by the drag due to the

466 background flow. If we fix all other parameters and increase Ω through positive values, the term

467 multiplying $\tilde{\varepsilon}$ in Eq. (12b) will become dominated by the Ω^2 term and will grow without bound

468 and the periodic trajectory may cease to exist. At the same time, a periodic orbit for the rigid

469 particle can always be found close to that of the fluid, regardless of the magnitudes of the

470 parameters Ω, a, b etc., provided that the relative particle size d/L (and thus $\tilde{\varepsilon}$), and/or the

471 relative density difference $\frac{(\rho_f - \rho_p)}{\rho_f}$ (and thus $\frac{3R}{2} - 1$) are made sufficiently small.

472 *Position of attracting periodic orbit; conditions for the loss of periodic orbit*

473 We have suggested that periodic orbits for rigid particles are encouraged when the $\tilde{\varepsilon} \left(\frac{3R}{2} - \right.$

474 $\left. 1 \right) \ll 1$, and in the case of Run 1 the value is 0.0066. A cross-sectional plot of the radial and

475 vertical components of the slow manifold particle velocity in a vertical section through the

476 cylinder (Fig. 4a) shows that the periodic orbit lies at $r = 0.369$ and $z = 0.504$ (as compared to

477 the values $r_c = 0.338$ and $z_c = 0.502$ predicted by Eq. (12). (The convergence of the

478 surrounding velocity field is too weak to be seen in the graphic.) If $\tilde{\varepsilon} \left(\frac{3R}{2} - 1 \right)$ is raised to the

479 moderately small value 0.02, the position of periodic trajectory migrates towards larger radius

480   (Fig. 4b), the reason being that the greater buoyancy (larger value of $\frac{3R}{2} - 1$) or smaller drag

481   (larger $\tilde{\varepsilon}$) requires a larger downward fluid velocity for equilibrium. Since the maximum

482   downward fluid velocity occurs at the outer cylinder wall (see Eq. (9c)) the position of the

483   periodic orbit continues to migrate outward and is lost (Fig. 4c) when $\tilde{\varepsilon}\left(\frac{3R}{2} - 1\right)$ exceeds a

484   value close to 0.3.

485   *Position of periodic orbit in numerical simulations:*

486   The slow-manifold reduction yields to the prediction (Eq. (12)) of the position of the attracting

487   material contour, or loop, for slightly buoyant particles. We can compare this prediction to what

488   is observed in numerical simulations using the Maxey-Riley Eqs. (1) and (2) over a range of

489   particle size d (and thus $\tilde{\varepsilon}$) and frame rotation Ω. As shown in Fig. 5, qualitative agreement with

490   the slow-manifold prediction, and the sketch in Fig. 3, holds for a very small d (when $\tilde{\varepsilon}$ is small).

491   Here the attractor in Fig. 5 is located close to the central periodic fluid parcel trajectory that lives

492   at mid-depth, $z = 0.5$ and $r = \frac{2R}{3} \approx 0.33$. As d (and $\tilde{\varepsilon}$) increases, the attractor moves

493   increasingly up and outward, and although the theory captures the trends, quantitative agreement

494   with the numerical results worsens. Also, when frame rotation Ω is increased (panel c), the

495   attractor responds by shifting up from mid-depth, again in qualitative but not quantitative

496   agreement with the slow-manifold prediction in Eq. (12b).

497   *Geometry of rigid particle trajectories and evidence of attraction in numerical simulations:*

498   If in the neighborhood of the periodic rigid particle trajectory $Q_a > 0$, the phase space for

499   buoyant particles will contract and the periodic trajectory becomes a candidate for an attractor of

500   such particles. An example of the attraction towards the periodic orbit is shown in Figure 2c,

501   where a set of slightly buoyant particles ($\frac{\rho_p}{\rho_f} = 0.97$) has been initialized over the volume of the

502   cylinder, and Eqs. (1) and (2) have been integrated forward in time to determine their subsequent

503   trajectories. Each trajectory is shown using a unique color. It can be seen that the particles

504   aggregate within a ring-like structure of decreasing thickness in the general vicinity of the

505   periodic orbit of the fluid flow.

506   *Basin of attraction – relationship to Q_a:*

507   To map out the basin of attraction for the particle periodic orbit, we first consider the region over

508   which phase space contraction for the buoyant particles (i.e. $Q_a > 0$) occurs. This region is

509   shown in Fig. 6a for the current example, along with the streamlines of the fluid overturning

510   stream function. Much of the fluid flow recirculates entirely within the region of positive Q_a,

511   whereas some of the outer streamlines cross the boundary (thick contour) between positive and

512   negative Q_a. If it were the case that rigid particles exactly followed streamlines of the fluid

513   overturning circulation, then net contraction or expansion of phase space along a rigid particle

514   trajectory would depend on the sign of the time-integrated value of Q_a along streamlines. The

515    $Q_a = 0$ contour, shown by a bold contour in each frame of Fig. 6, might then approximately

516   delineate the basin of attraction for buoyant rigid particles. In the slow-manifold approximation,

517   where rigid particle velocities lie close to the fluid velocities, the $Q_a = 0$ contour might continue

518   to do so.

519   To test this conjecture, we locate the basin of attraction in the numerical simulations by releasing

520   buoyant particles at various locations in the cross-section $0 < x < r_o$ and $0 < z < 1$, integrating

521   the subsequent trajectories over many overturning cycles, and recording the position (x_{final} and

522   z_{final}) of each particle where it crosses the same plane the final time (i.e., recording final

523   crossing with the Poincare section). We use the variable-step 4-th order Runge-Kutta integration

524 scheme, which we implemented in Matlab via the built-in function "ode45". In our simulations, the

525 relative and absolute tolerances are set to the value of 10^{-9} to integrate particle trajectories (Eqs.

526 (2) and (3)) (our results were not sensitive to the further decrease in tolerance values). Since the

527 flow (Eqs. (9a,b,c)) is prescribed analytically and has no normal flow component at the perimeter

528 and top and bottom of the cylinder, no interpolation scheme is needed and no extra boundary

529 conditions are enforced during the integration. Integration of a trajectory is stopped when a

530 particle got within one particle radius from the cylinder walls or top/bottom. The values of z_{final}

531 as a function of initial particle position are mapped in Fig. 7a, where the large green area

532 corresponding to $z_{final} \cong 0.5$ indicates the region from which particles are attracted. Only

533 particles initiated near the central axis of the cylinder, and close to the cylinder boundaries lie

534 outside this region, and these rise to the surface of the cylinder, contact the upper lid, and are no

535 longer followed. It can be seen that the green area in Fig. 7a has an oval shape that somewhat

536 resembles the overturning streamlines at small x in the central part of the cylinder, but extends to

537 near the top, bottom and outer cylinder boundaries at larger x. Thus the $Q_a = 0$ contour provides

538 a rough indication of the size and shape of the basin of attraction, but misses some important

539 details.

540 *Basin of attraction – dependence on* Ω

541 We have seen that the location of the periodic orbit that acts as an attractor for buoyant particles

542 shifts up and out in response to increasing frame rotation Ω (Fig. 5c). In Fig. 8 we indicate the

543 corresponding changes in the extent of the basin of attraction with respect to changing Ω by re-

544 computing Fig. 8a with $\Omega = 0.3, 1,$ and 10. The two smaller Ω values (0.3 and 1) correspond

545 roughly to Rossby numbers $a/2\Omega$ of about 1 and 0.2, i.e., are representative of the ocean

546 submesoscale and mesoscale flows. The Q_a-functions for these cases are plotted in Fig. 6b-c.

547   Most submesoscale eddies are going to tend to have $u^{(\theta)}/r$ about the same magnitude as Ω

548   (except on the equator) and mesoscale eddies will have $u^{(\theta)}/r \ll \Omega$. The results in Fig. 8

549   suggest that, while the basin of attraction does shrink slightly with increasing Ω, this dependence

550   is weak. The main difference between the three numerical runs in Fig. 8 is in the associated

551   attraction time, which gets significantly shorter for larger values of Ω. This is explored in more

552   detail below.

553   *Attraction time:*

554   It follows from Eq. (6) that the attraction time towards the periodic orbit should scale as $T_a =$

555     $\left[2\tilde{\varepsilon}\ \left(\frac{3R}{2} - 1\right) Q_a\right]^{-1}$ where $Q_a = \frac{1}{2}\left(\frac{1}{2}\left|\vec{\zeta}_a\right|^2 - |S|^2\right)$ with $\vec{\zeta}_a = \vec{\zeta}_r + \overrightarrow{2\Omega}$. Thus, for $\vec{\zeta}_r \geq 0$, as in

556   most of our numerical runs (except Experiment 1e), attraction time decreases with increasing Ω

557   for positive $\Omega \geq 0$. For negative $\vec{\zeta}_r$, which corresponds to the reversed direction of the flow in

558   our simulations (Experiment 1e), an increase in Ω will initially slow the attraction by decreasing

559   the magnitude of $\vec{\zeta}_a$ all the way to 0, at which point the periodic orbit will lose its attraction

560   properties, but then will speed up the attraction as Ω is further increased. This trend is confirmed

561   numerically in Fig. 9, where for the flow parameters corresponding to the "reversed flow" run in

562   Table 1 (Experiment 1e, with $\vec{\zeta}_r < 0$), we release a sample trajectory within the basin of

563   attraction and plot its z-coordinate as it winds around the can and eventually approaches the

564   attracting periodic orbit. As anticipated, the attraction time initially increases as Ω is increased

565   from 0 to 0.6, but then decreases as Ω is further increased to 2.

566   *Disappearance of the subsurface attractor when $\tilde{\varepsilon}$ becomes too large:*

567   Finally, to illustrate the disappearance of the subsurface attractor when $\tilde{\varepsilon}$ becomes too large, in

568   Fig. 10, we contrast 2 numerical simulations with the same flow parameters (corresponding to

569   the "slow overturn" run 1c in Table 1) but different particle diameters, $d = 10^{-3}$ vs $d = 5 \times$

570   10^{-4}. For larger d, the subsurface periodic orbit for rigid particles is no longer present within the

571   can, leading to all particles rising up to the surface (Fig. 10b). For smaller d, the periodic orbit is

572   still present and acts as an attractor for buoyant rigid particles over a significant portion of the

573   can (green region in Fig. 10a). We note that this run would be more qualitatively similar to the

574   oceanic mesoscale or submesoscale eddies, where the overturning component of circulation is

575   weak in comparison to the horizontal swirl.

576   (b) steady non-symmetrically perturbed case

577   We now consider a case in which the axial symmetry of the steady flow has been broken, here

578   through a change in the perturbation amplitude parameter ε from zero to 0.25, and in the offset

579   parameter y_o from 0 to -0.2 in the Eqs. (9a,b). The fluid velocity field now contains something

580   like a stationary, "mode-1" azimuthal wave in the horizontal velocity field.

581   The resulting Lagrangian structure (Fig. 2d and e) has a sea of chaos that covers the near-axial

582   and outer regions of the cylinder, where no unbroken tori survive. Within this chaotic sea is a

583   region containing a nest of unbroken tori that surround a central periodic orbit. This orbit has

584   evolved from the central periodic orbit of the symmetry case and is now tilted. Within the nest of

585   unbroken tori there exist resonant layers, in which new tori have arisen, and the most prominent

586   is the "island" that is centered near $x = 0.4$ and $z = 0.2$ in the right-half (and near $x = 0.4$ and

587    $z = 0.2$ in the right half) of Fig. (2d). We further note that this center lies within the region of

588   positive Q_a (Fig. 6b). The island corresponds to the yellow tori in Fig. 3e and is produced by a

589    $1:1$ resonance, so that the periodic trajectory running through its center executes one complete

590   azimuthal cycle and one overturning cycle before connecting back onto itself. Thus, in this

591   steady asymmetric configuration, we now have 2 periodic orbits of the fluid flow – the central

592 slightly-tilted periodic orbit near mid-depth (that evolved from the central horizontal periodic

593 orbit of the axisymmetric flow) and a new periodic orbit running through the center of the

594 resonant island (resulting from the break-up of the resonant torus satisfying $\Omega_{\tilde{\theta}} + \Omega_{\phi} = 0$).

595 We speculate that for sufficiently small $\tilde{\varepsilon}$ a periodic orbit for the rigid particle motion exists in

596 the vicinity of each of the 2 periodic orbits of the fluid flow. This conjecture is difficult to prove

597 due to a complex geometry, leading to centrifugal forces that act in different directions at

598 different locations along the particle path. For now we simply search for the supposed attractors

599 by releasing particles and following their trajectories.

600 As shown in Fig. 2f, separate attractors arise in the vicinity of two periodic orbits. The first

601 appears as a ring-like structure (purple core) lying near the center of the original nested tori and

602 the second is a similar feature with a red core near the center of the resonant island. The two are

603 chained together and each has its own basin of attraction (Fig. 7c): the first consisting of a

604 roughly elliptical patch (inner green region) in the x-z-plane, which corresponds of a slice

605 through a tube-like structure in 3D, and the second consisting on an annular (blue) region that

606 surrounds the green region and that occupies a relatively larger volume.

607 In order to check that attraction of slightly-buoyant rigid particles towards periodic orbits located

608 near the centers of the resonant islands in the perturbed flow is not limited to the case of the $1:1$

609 resonance, in an additional simulation (Fig. 11, experiment 2c in Table 1), we adjusted the

610 background flow parameter b in Eqs. (9), which is responsible for the overturning strength, to

611 create a $2:1$ resonance instead of a $1:1$ resonance, as in the original run. In this case, the

612 resonant torus breaks down giving rise to a 2-island chain on the corresponding Poincare section

613 (Fig. 11a), and the fluid periodic orbit that goes through the centers of both islands completes 2

614   full cycles in azimuth and 1 complete cycle in vertical before connecting onto itself. Also, as in

615   the original run, a second slightly-tilted periodic orbit still exists near mid-depth of the can.

616   When buoyant particles are released into this flow, two attractors arise, corresponding to the 2

617   periodic orbits of rigid particles – one near mid-depth (purple core in Fig. 11c) and another in red

618   near the center of the 2:1 resonant island.

619   *Shift in position of the periodic orbit associated with a resonant island as a function of flow and*

620   *particle parameters, and frame rotation*

621   The position of the attracting periodic orbit for rigid particles that is located within the resonant

622   islands (we will refer to it as the resonant periodic orbit) in the asymmetrically-perturbed flow

623   depends both on the perturbation strength (via ε), on the flow and particle parameters (via $\tilde{\varepsilon}$), and

624   on the frame rotation Ω. Specifically, this resonant periodic orbit for the rigid particles will shift

625   away from the corresponding periodic trajectory of the fluid flow as $\tilde{\varepsilon}$ and Ω are increased. The

626   same is true for the slightly-tilted central attracting periodic orbit near mid-depth. This is

627   qualitatively similar to the shifting of the central periodic orbit up and out from $z = 0.5$,

628    $r = 0.34$ in the axisymmetric flow in response to changing $\tilde{\varepsilon}$ and Ω, which we explored in detail

629   the previous section both analytically (Eqs. (12)) and numerically (Fig. 3-5).

630   In order to numerically illustrate the shift in the position of the attracting periodic orbits, we

631   present (Figs. 12 and 13) numerical simulations in the steady perturbed flow configuration for 3

632   values of d (and thus $\tilde{\varepsilon}$) and 3 values of Ω. As both parameters increase, the attractors move

633   away from the corresponding periodic orbits of the fluid flow. This shift is evident from the

634   change in the color of the attraction basins in (a,d,g) and from the location of the yellow cloud of

635   dots in (c,f,i) in Figs. 12-13. Increases in $\tilde{\varepsilon}$ and Ω also lead to the shrinkage of the attraction

636   basins for both attractors and to a faster convergence rate, as is evident from the tighter cloud of

637   yellow dots in (c,f,i), as discussed in more detail below. The basin of attraction for the central

638   attractor – the green region in Fig. 12 – seems to shrink faster than the basin of attraction for the

639   resonant attractor (the blue-ish region) as d increases, so when d is increased from 2×10^{-3} to

640   3×10^{-3}, the central attractor vanishes, whereas the resonant attractor is still present (Fig. 12g).

641   On the other hand, the increase in Ω (Fig. 13) causes a faster shrinkage of the basin of attraction

642   for the resonant attractor than for the central attractor, so when Ω is increased from 2 to 5 in Fig.

643   13g, the resonant attractor disappears, whereas the central attractor is still present. Figs. 12g,h,i

644   (and Fig. 13g,h,i) show cases where this threshold has been exceeded, and one of the attractors

645   has been lost, whereas the other is still present.

646   *Attraction time:*

647   Similar to the unperturbed flow, the attraction time for attractors in the steady, perturbed flow

648   may still scale as $T_a = \left[2\tilde{\varepsilon}\left(\frac{3R}{2} - 1\right)Q_a\right]^{-1}$, provided that Q_a is regarded as a typical value

649   within the corresponding basin of attraction. The predicted decrease in attraction time with

650   increasing $\tilde{\varepsilon}$ and Q_a is evident from the numerical simulations in Figs. 12-13, where in (c,f,i) we

651   color-coded trajectory crossings with the x-z Poincare plain by time, with blue/yellow

652   corresponding to initial/final time. For smaller values of $\tilde{\varepsilon}$ and Ω, we observe a wider and more

653   diffuse cloud of dots (because trajectories wind around the can many times before approaching

654   the attractor), whereas as $\tilde{\varepsilon}$ and Ω increase, the clouds at comparable times become denser and

655   more compact around the attractors.

656   *Basin of attraction*

657 For the slightly-tilted central periodic orbit located within the central non-chaotic region near

658 mid-depth in Fig. 2f, we observe that the basin of attraction – green region in Fig. 7b – extends

659 roughly from the location of the periodic orbit to the edge of the central non-chaotic region (that

660 is foliated by discretely sampled closed curves in Fig. 2d). Note that as $\tilde{\varepsilon}$ increases, the attracting

661 periodic orbit moves away from the center of this non-chaotic region towards its edge, leading to

662 the shrinkage and eventual disappearance of the corresponding basin of attraction, shown by the

663 green regions in Fig. 12a,d,g).

664 Similarly, in all of our numerical simulations, we observe that for the resonant attracting periodic

665 orbit running through the resonant islands, the basin of attraction seems to cover the region

666 between the orbit and the edge of the corresponding resonant island. An analytical expression for

667 the width of the (non-degenerate) resonant island in the fluid flow (Pratt et al., 2014) predicts

668 that $\Delta I = \sqrt{\dfrac{\epsilon F_{nm}^0(I_0)}{\left(n\frac{d^j\Omega_\phi}{dI^j}+m\frac{d^j\Omega_\theta}{dI^j}\right)_{I_0}}}$, where ΔI is the deviation in the action coordinate away from I_0, the

669 value of action at the resonant torus (i.e., at the center of the island). This width depends on the

670 strength of the perturbation ϵ, the order of the resonance (via n and m in the resonance

671 condition), the background flow (via $\frac{d^j\Omega_{\phi/\theta]}}{dI^j}$), and the structure of the perturbation (via $F_{nm}^0(I_0)$).

672 This expression could be used as an upper limit on the extent of the basin of attraction. However,

673 because the attracting periodic orbit will move away from the center of the island towards its

674 edge as $\tilde{\varepsilon}$ and Ω increase, the basin of attraction for the resonant attractor (blue region in Figs.

675 12a,d and 13a,d) becomes increasingly smaller than ΔI. One might speculate, then, that the

676 attractor will completely disappear when the attracting periodic orbit reaches the edge of the

677 resonant island. This is the case in Figs. 13g where the resonant attractor is no longer present.

678   (c) non-steady, non-symmetrically perturbed case

679   The final case that we will consider is one in which the perturbation is asymmetric and varies

680   periodically in time. The chosen perturbation frequency, $\sigma = 2\pi/9.1$, causes 2 strong additional

681   resonances (compared to the steady perturbed case) – one with $n = 0$, $m = 1$, and $l = 1$ (i.e.,

682   with a torus whose overturning frequency is equal to the perturbation frequency) that is shown in

683   blue in Fig. 2g,h and is located near the outer edge of the central non-chaotic region, and another

684   resonance, shown in green in Fig. 2g,h, with $n = 1$, $m = 1$, and $l = 1$, which is located between

685   the central non-chaotic region and the larger $n = 1$, $m = 1$ resonant island (that was present in

686   the steady case as well). Both of these new resonant structures are time dependent, their shape

687   and position recurring periodically. For example, the blue island, which looks like a crescent

688   moon pointing upward on the Poincare section at $t = 0$, becomes a crescent moon pointing

689   downward at time 4.55. The movement of the green island is more complex, as it turns both in

690   azimuth and vertical, making one complete loop over 9.1 time units. Because of the time-

691   dependence, trajectories must be strobed at the forcing frequency σ in order to capture

692   'snapshots' of their forms as they recur at a particular phase in the time cycle. At the center of

693   each feature is a closed material curve that also varies periodically. Where the island has

694   emerged from the breakup of a torus with quasiperiodic orbits, the individual trajectories that

695   populate the material curves are themselves quasiperiodic.

696   Particle trajectory computations in this case confirm that the purple, red and green islands give

697   rise to attractors (Fig. 3i), whereas the blue island does not. In fact, slightly-buoyant rigid

698   particles that are released in the blue region converge towards the attractor that lies near the

699   purple region. This is also indicated by the basin of attraction of the central attractor extending

700   across the space occupied by the blue resonant island in Fig. 7c.

IV.   Discussion

We have considered attraction phenomena for small, finite size, spherical, buoyant, rigid particles in a three-dimensional rotating cylinder flow with azimuthal rotation and overturning, and both with or without time dependence. The aim has been to gain insights into the behavior of slightly buoyant microplastic particles in 3D vortex flows that qualitatively resemble ocean eddies. The rigid particle motion is governed by a simplified version of the Maxey-Riley equations (accounting for inertia, buoyancy and simplified quantification of drag and added mass), and, approximately, by the slow-manifold reduction of these equations. We have illustrated the possibility of aggregation of slightly-buoyant rigid particles in 3D vortex flows towards closed loop attractors located subsurface within the interior of the flow. Even in our idealized flow and for spherical particles with fixed radius and buoyancy, aggregation is non-trivial, often with multiple attractors present and/or the lack of attraction in some circumstances.

Our rotating cylinder model is much less complex than any real ocean eddy in many respects, including the assumed quasiperiodic time dependence and the absence of decay and interaction with the surroundings. Understanding aggregation in a simple periodic flow seems like a reasonable first step towards understanding aperiodic, interacting, and decaying oceanic eddies. This approach is common in applications of dynamical systems theory to oceanography and meteorology. For example, arguments relating to the increased stability of jets due to the strong Kolmogorov-Arnold-Moser stability near shearless trajectories have first been developed for spatially-periodic and time-quasiperiodic flows and tested using idealized toy models, before exploring these ideas in more realistic oceanic and atmospheric settings (see Rypina et al., 2007 and Beron et al., 2008; 2010). Note also that our results are applicable to quasi-periodic disturbances with finite number of frequencies rather than just periodic disturbances (we only

724 show numerical simulations for the time-periodic case for simplicity), and a quasiperiodic

725 function might potentially be useful for approximating temporal variability in some oceanic

726 flows, especially those with pronounced peaks in the spectrum.

727 We have explored a steady axisymmetric rotating cylinder flow and a steady flow with its axial

728 symmetry broken. In all cases, we have observed emergence of subsurface attracting structures

729 that lead to the aggregation of buoyant particles towards them. We have linked these attractors to

730 the periodic orbits of rigid particles that exist in a region of net contraction of the phase space of

731 the particle motion. The slow manifold equations suggest that periodic orbits for rigid particles

732 exist near periodic orbits of the underlying fluid flow, provided the drag is sufficiently strong

733 (Stokes number $<<$ 1).

734 We have also explored one case of an axially asymmetric and time-periodic flow, with focus on

735 the resonant "islands" that arise due to the time-dependence. At the center of such islands are

736 closed material contours, or loops, composed of quasi-periodic orbits of the fluid flow. One such

737 structure has a nearby attractor, also a closed loop of quasiperiodic orbits for rigid particles,

738 while a second example does not. A detailed explanation awaits formulation of a quantitative

739 theory, something that is beyond the scope of the present paper and that will be presented in a

740 future work.

741 We have observed that the disappearance of an attractor, which can occur as the result of

742 increasing rigid particle size or frame rotation, coincides roughly with the displacement of the

743 position of the attractor to the outer edge of the resonant island from which it sprang. Whether

744 this purely geometric observation forms the basis for a general criterion for the loss of attraction

745 is unknown, as a dynamical justification is needed.

Marine microplastics can have complex non-spherical tangled-filament shapes, change their physical and chemical properties in time due to aging and photo- or chemical-decay processes (Andrady 2011), are subject to biofouling (see recent relevant work by Kreczak et al., 2021), and may interact leading to the formation of clusters. None of these effects were considered in this paper, and all will need to be taken into account for the realistic prediction of marine microplastic evolution and re-distribution in the ocean. Real ocean eddies are also decaying in time and are usually moving (translating) rather than stationary. Translation with a constant velocity can be handled by considering the flow in a moving frame of reference, but decay and interactions will likely change the geometry of the circulation and make the flow truly aperiodic. Our simplified model cannot account for these effects, which will need to be explored separately later.

Acknowledgements: Work supported by the NSF grant OCE# 2124210 and ONR CALYPSO grants #N000141812417 and #N000141812165.

Data Availability Statement: No observational data was used. Details of the numerical simulations using an analytical vortex model are provided in text.

Author Contribution Statement: IR led the overall effort and performed most of the numerical simulations, LP contributed towards the theoretical understanding and interpretation of the results, MD participated in the overall effort.

Competing interests Statement: no competing interests

References

Andrady, A.L., 2011. Microplastics in the marine environment. *Marine pollution bulletin*, *62*(8), pp.1596-1605.

Basset, A. B. (1988). Treatise on Hydrodynamics, Deighton Bell, London, Vol. 2, Chap. 22, pp. 285-297.

Beron-Vera, F. J., M. G. Brown, M. J. Olascoaga, I. I. Rypina, H. Kocak, and I. A. Udovydchenkov (2008). Zonal jets as transport barriers in planetary atmospheres. *Journal of Atmospheric Science*, 65, 3316-3326.

Beron-Vera, F. J., M. J. Olascoaga, M. G. Brown, H. Kocak, and I. I. Rypina (2010). Invariant-tori-like Lagrangian coherent structures in geophysical flows. *Chaos*, 20, 017514, doi:10.1063/1.3271342.

Beron-Vera, F. J., M. J. Olascoaga and R. Lumpkin, 2016. Inertia-induced accumulation of flotsam in the subtropical gyres. Geophys. Res. Lett., 43, 12228-12233, https://doi.org/10.1002/2016g1071443.

Beron-Vera, F. J., M. J. Olascoaga and P. Miron, 2019. Building a Maxey-Riley framework for surface ocean inertial particle dyamics. Phys. Fluids 31; doi: 10.1063/l.5110731.

Beron-Vera, F.J., 2021. Nonlinear dynamics of inertial particles in the ocean: From drifters and floats to marine debris and Sargassum. *Nonlinear dynamics*, *103*(1), pp.1-26.

Boussinesq, J. (1903) Theorie Analytique de la Chaleur, L'Ecole Polytechnique, Paris, Vol.2, p. 224.

787 Brandt, L. and F. Coletti (2022) Particle-Laden Turbulence: Progress and Perspectives. Ann.

788   Rev. Fluid Mich. 54, 159-189. https://doi.org/10.1146/annurev-fluid-030121-021103

789 Choy, C.A., Robison, B.H., Gagne, T.O., Erwin, B., Firl, E., Halden, R.U., Hamilton, J.A.,

790   Katija, K., Lisin, S.E., Rolsky, C. and S. Van Houtan, K., 2019. The vertical distribution and

791   biological transport of marine microplastics across the epipelagic and mesopelagic water

792   column. *Scientific reports*, *9*(1), p.7843.

793 Daitche, A. and Tél, T., 2011. Memory effects are relevant for chaotic advection of inertial

794   particles. *Physical review letters*, *107*(24), p.244501.

795 Delandmeter, P. and E. van Sebille (2019). The Parcels v2.0 Lagrangian framework: new field

796   interpolation schemes. Geosci. Model Dev. Discuss., https://doi.org/10.5194/gmd-2018-339

797 DiBenedetto, M. H., N. T. Ouellette, and J. R. Koseff, 2018a. Transport of anisotropic particles

798   under waves. J. Fluid. Mech. 837, 320-340, doi:10.1017/jfm.2017.853.

799 DiBenedetto, M.H. and Ouellette, N.T., 2018b. Preferential orientation of spheroidal particles in

800   wavy flow. *Journal of Fluid Mechanics*, *856*, pp.850-869.

801 Faxén, H., 1922. Der Widerstand gegen die Bewegung einer starren Kugel in einer zähen

802   Flüssigkeit, die zwischen zwei parallelen ebenen Wänden eingeschlossen ist. *Annalen der*

803   *Physik*, *373*(10), pp.89-119.

804 Fountain, G.O., Khakhar, D.V., Mezić, I. and Ottino, J.M., 2000. Chaotic mixing in a bounded

805   three-dimensional flow. *Journal of Fluid Mechanics*, *417*, pp.265-301.

806 Froyland, G., Stuart, R. M., & van Sebille, E. (2014). How well-connected is the surface of the

807   global ocean?. *Chaos*, 24(3), 033126. https://doi.org/10.1063/1.4892530

Fenichel, N.: Geometric singular perturbation theory for ordinary differential equations. J. Differ. Equ. 31, 51–98 (1979)

Gatignol, R., 1983. The Faxén formulae for a rigid particle in an unsteady non-uniform Stokes flow.

Greenspan, H. P., 1968. *The theory of rotating fluids* (Vol. 327). Cambridge: Cambridge University Press.

Haller, G., and T. Sapsis, 2008. Where do inertial particles go in fluid flows? Physica D, 237, 573-583.

Hart, J.E. and Kittelman, S., 1996. Instabilities of the sidewall boundary layer in a differentially driven rotating cylinder. *Physics of Fluids, 8*(3), pp.692-696.

Kelly, R., D. B. Goldstein, S. Suryanarayanan, M. B. Tornielli and R. A. Handler, The nature of bubble entrapment in a Lamb-Oseen vortex. Phys. Fluids 33, 061702; https://doi.org/10.1063/5.0053658.

Kooi, M., Reisser, J., Slat, B., Ferrari, F.F., Schmid, M.S., Cunsolo, S., Brambini, R., Noble, K., Sirks, L.A., Linders, T.E. and Schoeneich-Argent, R.I., 2016. The effect of particle properties on the depth profile of buoyant plastics in the ocean. *Scientific reports, 6*(1), p.33882.

Kreczak, H., Willmott, A.J. and Baggaley, A.W., 2021. Subsurface dynamics of buoyant microplastics subject to algal biofouling. *Limnology and Oceanography, 66*(9), pp.3287-3299.

Kukulka, T., Proskurowski, G., Morét-Ferguson, S., Meyer, D. W., & Law, K. L.(2012). The effect of wind mixing on the vertical distribution of buoyant plastic debris. *Geophysical

Research Letters, 39, L07601. https://doi.org/10.1029/2012GL051116

Kvale, K., Prowe, A.F., Chien, C.T., Landolfi, A. and Oschlies, A., 2020. The global biological microplastic particle sink. *Scientific reports*, *10*(1), p.16670.

Lackey, T.C. and Sotiropoulos, F., 2006. Relationship between stirring rate and Reynolds number in the chaotically advected steady flow in a container with exactly counter-rotating lids. *Physics of Fluids*, *18*(5).

Landrigan PJ, Raps H, Cropper M, Bald C, Brunner M, Canonizado EM, Charles D, Chiles TC, Donohue MJ, Enck J, Fenichel P, Fleming LE, Ferrier-Pages C, Fordham, R, Gozt A, Griffin C, Hahn ME, Haryanto B, Hixson R, Ianelli H, James BD, Kumar P, Laborde A, Law KL, Martin K, Mu J, Mulders Y, Mustapha A, Niu J, Pahl S, Park Y, Pedrotti M-L, Pitt JA, Ruchirawat M, Seewoo BJ, Spring M, Stegeman JJ, Suk W, Symeonides C, Takada H, Thompson RC, Vicini A, Wang Z, Whitman E, Wirth D, Wolff M, Yousuf AK, Dunlop S. The Minderoo-Monaco Commission on Plastics and Human Health. *Annals of Global Health*. 2023; 89(1): 23, 1–215. DOI: https://doi. org/10.5334/aogh.4056

Lange, M. and E. van Sebille (2017) Parcels v0.9: prototyping a Lagrangian ocean analysis framework for the petascale age. Geosci. Model Dev., 10, 4175-4186. https://doi.org/10.5194/gmd-10-4175-2017

Langlois, G.P., Farazmand, M. and Haller, G., 2015. Asymptotic dynamics of inertial particles with memory. *Journal of nonlinear science*, *25*, pp.1225-1255.

Ledwell, J. R., McGillicuddy, D. J., and Anderson, L. A., "Nutrient flux into an intense deep chlorophyll layer in a mode-water eddy," Deep Sea Res., Part II 55, 1139–1160 (2008).

850 Maxey, M.R. and J. J. Riley, 1983. Equation of motion for a small rigid sphere in a nonuniform

851   flow. Phys. Fluids 26, 883.

852 Mountford, A. S. and M. A. Morales Maqueda (2019) Eulerian Modeling of the

853   Three=Dimensional Distribution of Seven Popular Microplastic Types in the Global Ocean.

854   *J. Geophys. Res*.: Ocean, 124, 8558-8573. https://doi:10.1029/2019JC015050.

855 Onink, V., Wichmann, D., Delandmeter, P., and van Sebille, E., 2019: The role of Ekman

856   currents, geostrophy and Stokes drift in the accumulation of floating microplastic, Journal of

857   Geophysical Research: Oceans, 124, 1474-1490, https://doi.org/10.1029/2018JC014547,

858 Okubo, A., 1970, June. Horizontal dispersion of floatable particles in the vicinity of velocity

859   singularities such as convergences. In *Deep sea research and oceanographic abstracts* (Vol.

860   17, No. 3, pp. 445-454). Elsevier.

861 Pabortsava, K. and Lampitt, R.S., 2020. High concentrations of plastic hidden beneath the

862   surface of the Atlantic Ocean. *Nature communications*, *11*(1), p.4073.

863 Pedlosky, J. and Spall, M.A., 2005. Boundary intensification of vertical velocity in a β-plane

864   basin. *Journal of physical oceanography*, *35*(12), pp.2487-2500.

865 Pratt, L. J., I. I. Rypina, T. Özgökmen, H. Childs, and T. Bebieva, 2014. Chaotic Advection in a

866   Steady, 3D, Ekman-Driven Circulation. *J. Fluid Mech*, 738, 143-183,

867   DOI:10.1017/jfm.2013.583.

868 Ripa, P., 1987. On the stability of elliptical vortex solutions of the shallow-water

869   equations. *Journal of Fluid Mechanics*, *183*, pp.343-363.

870 Rypina, I. I., M. G. Brown, F. J. Beron-Vera, H. Kocak, M. J. Olascoaga, and I. A.

Udovydchenkov (2007). Robust transport barriers resulting from strong Kolmogorov-Arnold-Moser stability. *Physical Review Letters*, 98, 104102, doi:10.1103/PhysRevLett.98.104102.

Rypina, I. I., L. J. Pratt, P. Wang, T. M. Ozgokmen, and I. Mezic, 2015. Resonance phenomena in a time-dependent, three-dimensional, Ekman-driven eddy. *J. Chaos*., 25, 087401, http://dx.doi.org/10.1063/1.4916086.

Shamskhany, A., Z. Li, P. Patel and S. Karimpour, 2021. Evidence of Microplastic Size Impact on Mobility and Transport in the Marine Environmnet: A Review and Synthesis of Recent Research. Front. Mar. Sci. 8:760649. Doi: 10.3389/fmars.2021.760649.

Stokes, G. G. (1851) Trans. Camb. Phil. Soc. 9, 8. (*Mathematical and Physical Papers* 3,1.)

Tchen, C. M. (1947). Ph. D. thesis, Delft, Martinus Nijhoff, The Hague/

van Sebille E., C. Wilcox, L. Lebreton, N. Maximenko, B.D. Hardesty, J.A. van Franeker, M. Eriksen, D. Siegel, F. Galgani, K.L. Law (2015) A global inventory of small floating plastic debris Environ. Res. Lett., 10 (2015), p. 124006, 10.1088/1748- 9326/10/12/124006

Wichmann, D., P. Delandmeter and E. van Sebille, 2019. Influence of Near-Surface Currents on the Global Dispersal of Marine Microplastics. J. Geophys. Res. (Oceans), 124(8), https://doi.org/10.1029/2019JC015328

Weiss, J., 1991. The dynamics of enstrophy transfer in two-dimensional hydrodynamics. *Physica D: Nonlinear Phenomena*, *48*(2-3), pp.273-294.

Experiment	a	b	ε	y_o	σ	γ	β	Ω	d
1 – steady symmetric	0.62	7.5	0	0	0	0	0	0	10^{-3}
1a (small Ω)	0.62	7.5	0	0	0	0	0	0.3	10^{-3}
1b (large Ω)	0.62	7.5	0	0	0	0	0	1	10^{-3}
1c (slow overturn)	0.62	0.25	0	0	0	0	0	1	10^{-3} vs. 5×10^{-4}
1d ($z_{attractor}$ vs Ω)	0.62	7.5	0	0	0	0	0	Sweep 0 to 10	10^{-3}
1e (reversed flow)	-0.62	-7.5	0	0	0	0	0	0, 0.6, 2	10^{-3}
2 – steady asymmetric	0.62	7.5	0.25	-0.2	0	0	0	0	10^{-3}
2a (small Ω)	0.62	7.5	0.25	-0.2	0	0	0	0.3	10^{-3}
2b (large Ω)	0.62	7.5	0.25	-0.2	0	0	0	1	10^{-3}
2c (2:1 resonance)	0.62	3.8	0.25	-0.2	0	0	0	0	10^{-3}
3 - non-steady asymmetric	0.62	7.5	0.25	-0.2	$\dfrac{2\pi}{9.1}$	0.2	1	0	10^{-3}

Table 1: Dimensionless parameter values for numerical experiments. Fixed parameters in the kinematic model (Eqs. 9a-c) are $c = 0.69$, and $r_0 = 1/2$ in all cases. Parameters that appear in the nondimensional Maxey-Riley Eq. (3) are also nondimensional, with $L, U, L/U$ as length, velocity and time scales. Fixed parameter values based on $L = 1$m and $U = 1$m/s include

$\dfrac{\rho_p}{\rho_f} = 0.97$, $R = \dfrac{2\rho_f}{\rho_f + 2\rho_p} = 0.680$, $\dfrac{3R}{2} - 1 = .020$ $\vec{g}_r = \dfrac{gL}{U^2} = 10.0$, $\tilde{\varepsilon} = \dfrac{2}{9}\left(\dfrac{d}{L}\right)^2 \dfrac{UL}{\nu} \dfrac{1}{R} = 0.33$, and

$\tilde{\varepsilon}\left(\dfrac{3R}{2} - 1\right) = 0.0067$. Note that $\vec{\Omega} = \Omega\vec{k} = \dfrac{\vec{\Omega^*}L}{U}$.
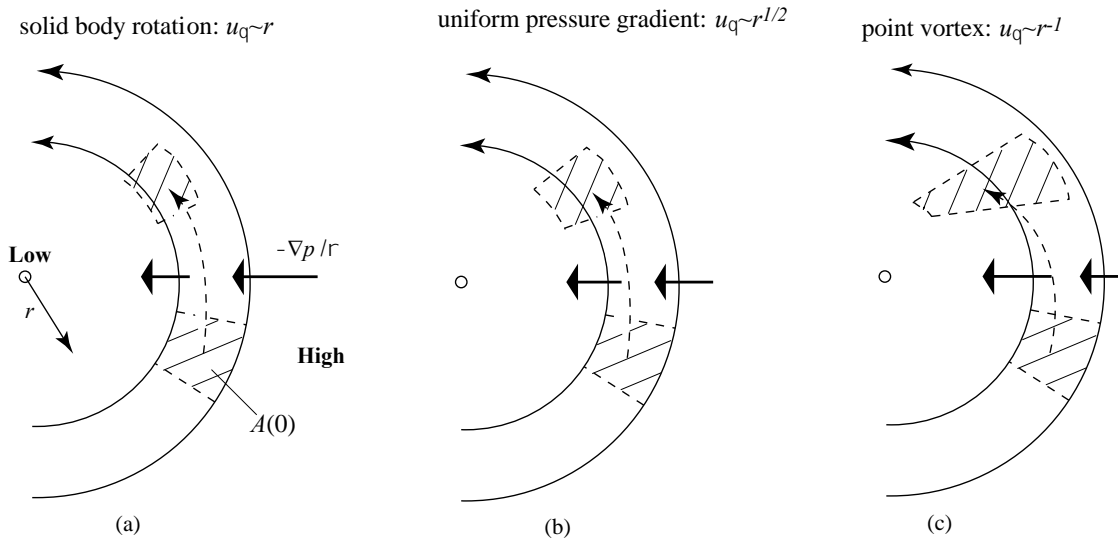
897

898   Figure 1. Three types of two-dimensional eddies with zero frame rotation and for which gravity

899   is imagined to be zero: solid body rotation (a), constant pressure gradient (b), and point vortex

900   (c). In each case, the cross hatched area represents a concentration of rigid particles with area

901    $A(t)$.

902

903

904

905

906

907

908

909

910
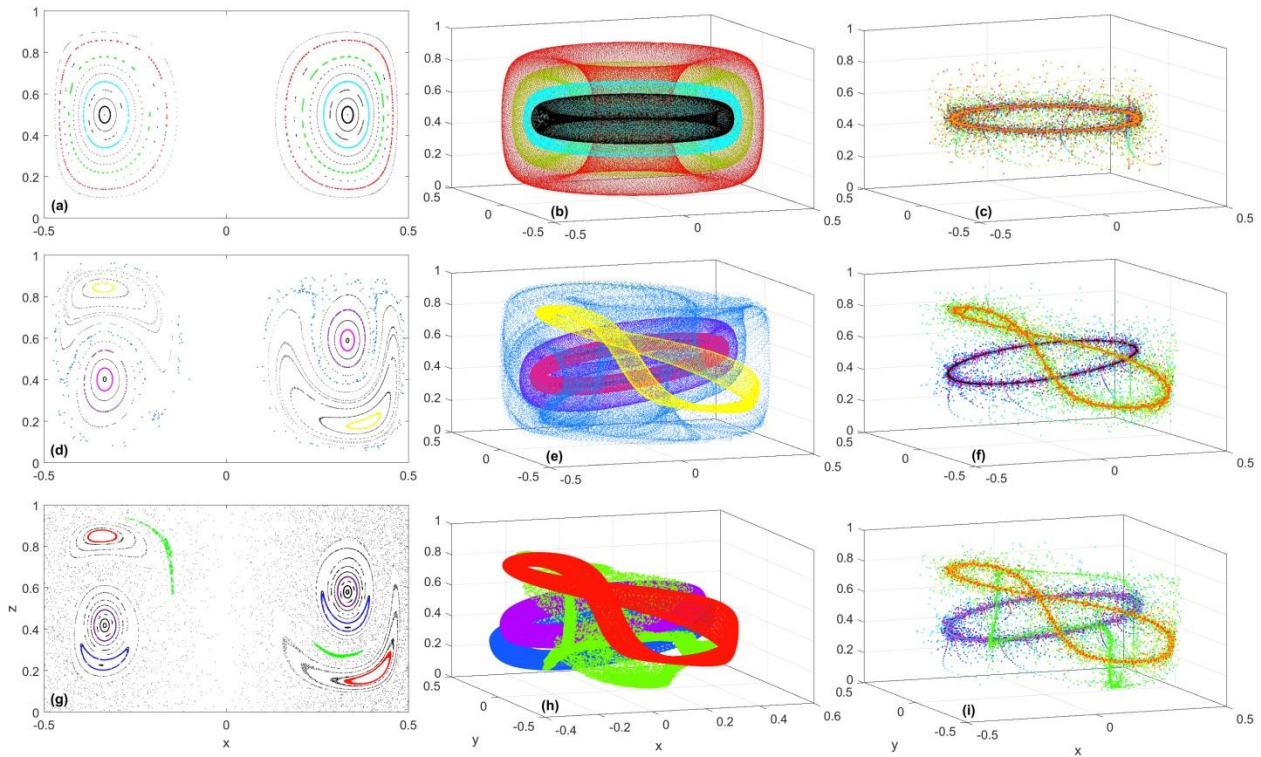
Figure 2. (left) Poincare section, (middle) fluid parcels trajectories in 3D, (right) buoyant particle

trajectories in 3D for a steady symmetric fluid flow (top row), steady asymmetric flow (middle

row), and non-steady, asymmetric flow. Parameter setting are listed under Experiments 1, 2 and

3 in Table 1. Colors in the left column of panels match the corresponding panel in the middle

column, but the colors in the right column indicated time after release of the particles. Note the

attraction of buoyant particles to a single attractor at mid-depth in panel (c), to 2 attractors in

panel (f), and to 3 attractors in panel (i). Particles are released along a vertical line $x = 0.334$,

$y = 0$, $0 < z \leq 0.6$ with initial velocity equal to that of the co-located fluid parcels.

919

920

921
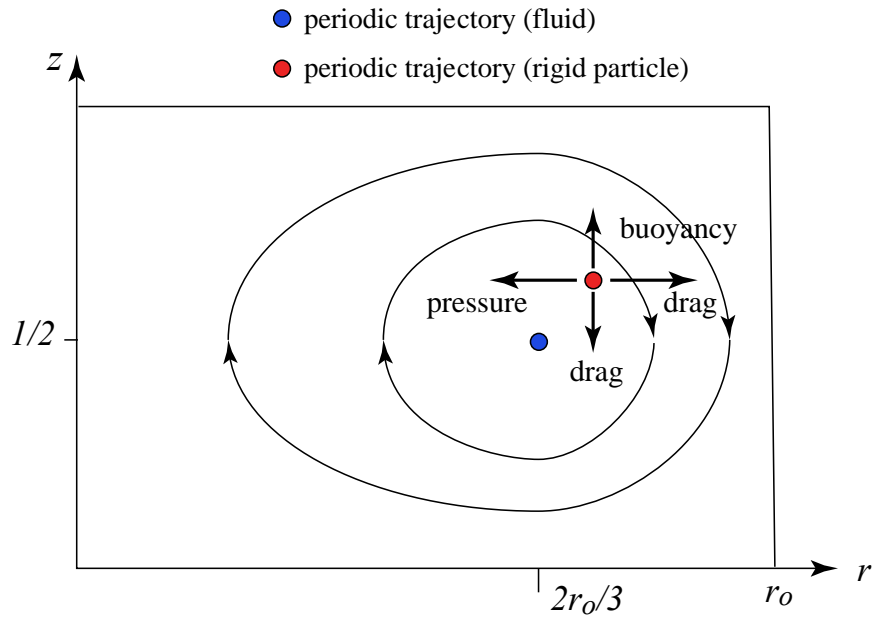
922

923 Figure 3. Sketch showing the position in a vertical section of the periodic orbit (red dot) of the

924 rigid particle relative to the periodic orbit (blue dot) of the fluid flow. The viewer sees one half

925 of a vertical slide though the cylinder, with the azimuthal flow directed away from the viewer

926 and the cylinder center at the left edge.

927

928

929

930

931

932

933

934
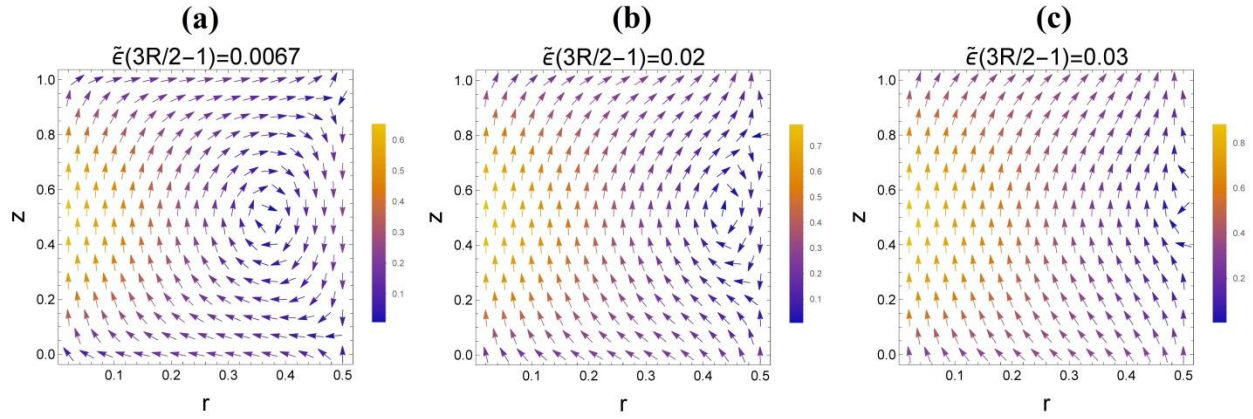
Figure 4. The slow-manifold radial and vertical velocity components for the rigid particles,

plotted in the (r, z) plane for (a) $\tilde{\varepsilon}\left(\frac{3R}{2} - 1\right) = 0.0067$, (b) $= 0.02$, and (c) $= 0.03$. Other

parameters are as listed for Experiment 1a in Table 1.

935

936

937

938

939

940

941

942

943

944

945

946

947
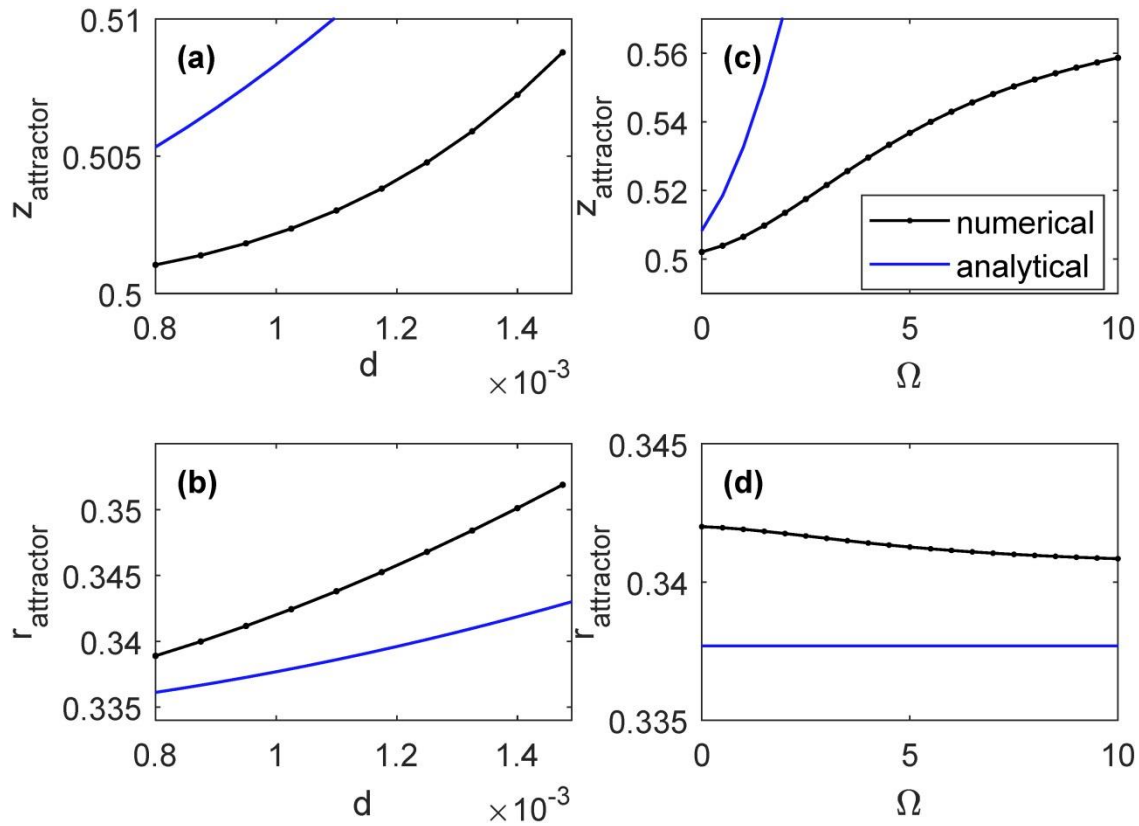
948

949 Figure 5. For the steady symmetric rotating cylinder flow, the coordinates of the periodic orbit

950 that acts as an attractor for buoyant particles as a function of particle diameter (a-b) and frame

951 rotation (c). Flow parameters are listed in Table 1 and correspond to Experiment 1 for (a-b) and

952 Experiment 1d for (c-d).

953

954

955

956

957

958
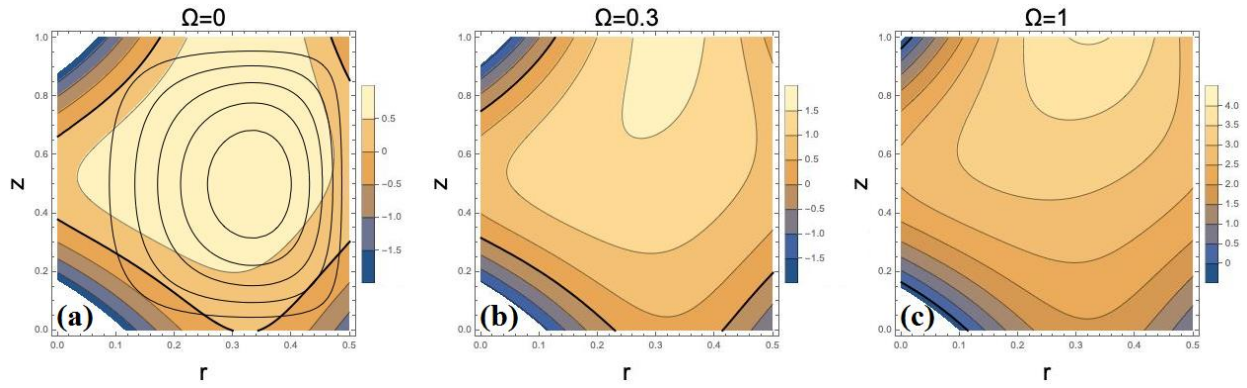
Figure 6. (a): The Q_a function for the steady, axisymmetric, cylinder flow with the same

parameter setting (see Experiment 1a) as for Figure 3a-c, and plotted in (*x*,*z*) along with the

streamlines of the overturning circulation. The thick rigid curve corresponds to $Q_a = 0$. (b): The

same parameter settings, except Ω has been raised from 0 to 0.3 (Rossby number $\cong 1$)   (c):

$\Omega = 1.0$. (Rossby number $\cong 0.2$).

964

965

966

967

968

969

970

971

972
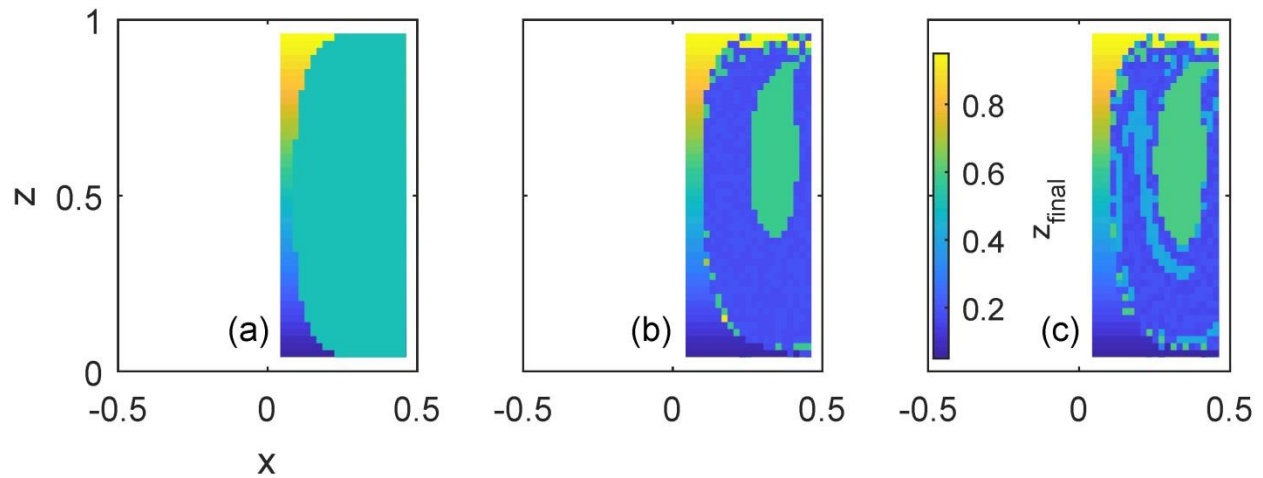
973

974   Figure 7. Domain of attraction for the attractors in (a) steady symmetric (Experiment 1 in Table

975   1), (b) steady asymmetric (Experiment 2 in Table 1), and (c) time-periodic asymmetric rotating

976   cylinder flow (Experiment 3 in Table 1). (These are the same 3 experiments that were used to

977   produce Fig. 2.) The color indicates the height (i.e., value of z-coordinate) of the final crossing of

978   a trajectory with the Poincare section, as a function of particle's release location. Particles

979   attracted to the same attractor thus correspond to same color.

980

981

982

983

984

985

986

987
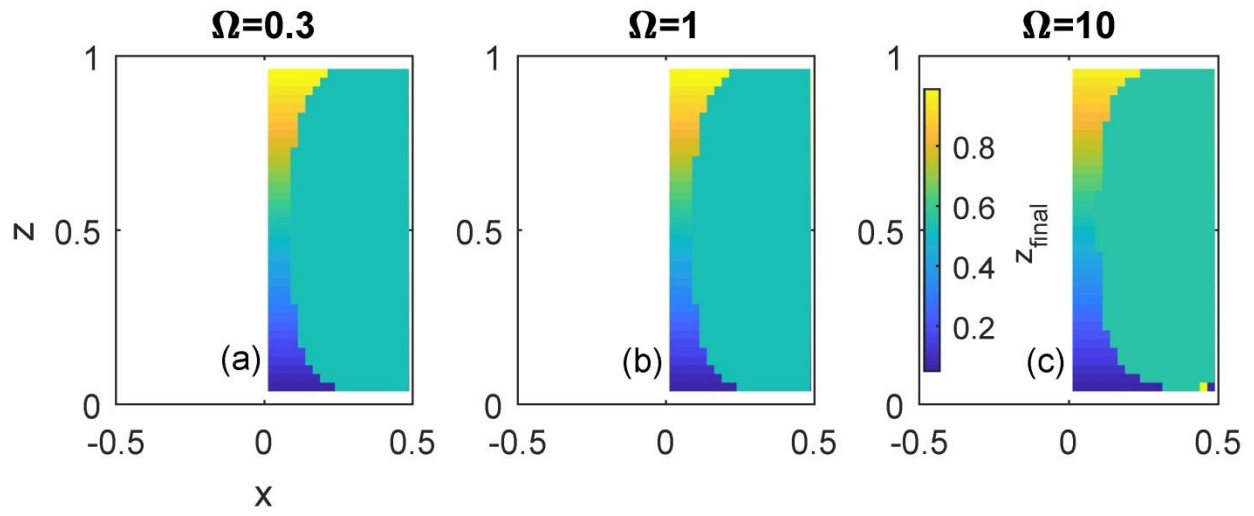
Figure 8. Same as in Fig. 7a but with frame rotation.

988

989

990

991

992

993

994

995

996

997

998

999
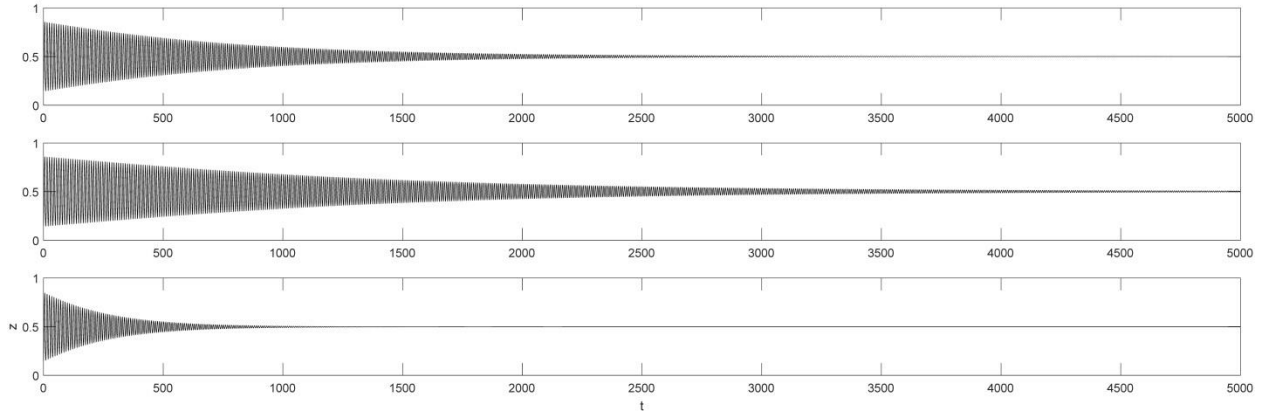
Figure 9. For the "reversed flow" experiment (Experiment 1e in Table 1), z-position of a sample

particle trajectory as function of time for 3 values of Ω: 0 (top), 0.6 (middle), and 2 (bottom).

Time t is in dimensionless units (but since our scaling coefficient for time is equal to 1 sec, the

numbers on the x-axis can also be read as dimensional time in sec.)

1013
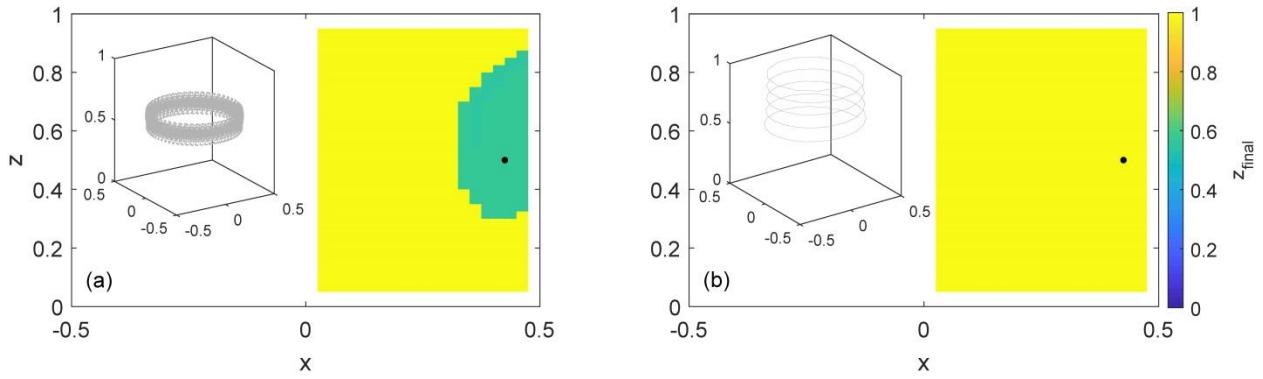
Figure 10. For the "slow overturn" Experiment 1c from Table 1, color indicates the final z-

coordinate of a particle's trajectory at the end of integration time as a function of particle's

release location for 2 values of d: (a) 5×10^{-4} and (b) 10^{-3}. Yellow corresponds to particles

rising up to the top, whereas green indicates the basin of attraction of the subsurface attracting

periodic orbit. The insets at the left side of each frame show a sample trajectory whose release

location is indicated by the black dot.

1028
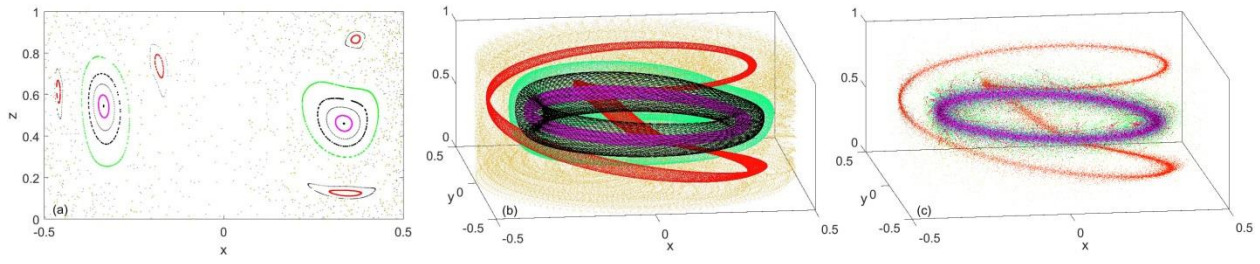
1029

1030   Figure 11. Same as Fig. 2(d-f) but with $b = 3.8$.

1031

1032

1033

1034

1035

1036

1037

1038

1039

1040

1041

1042
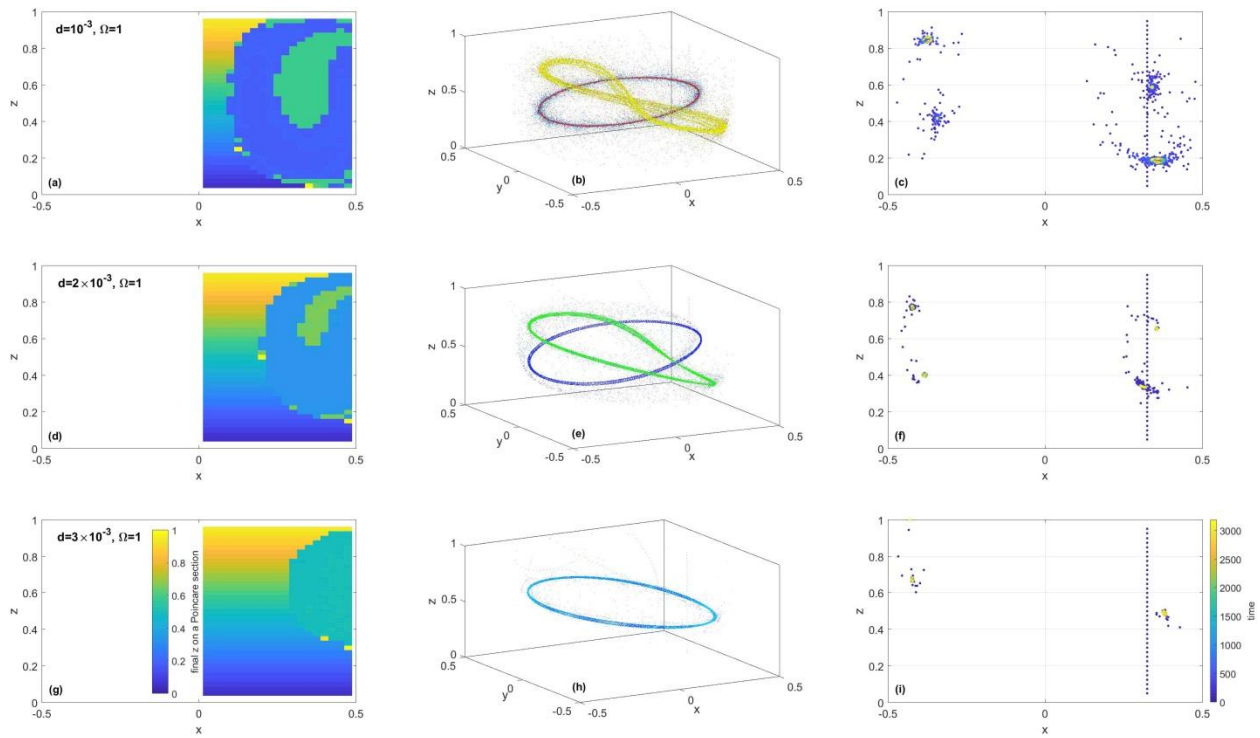
1043

Figure 12. For the steady perturbed system (Experiment 2 in Table 1), changes in the location of

the attracting periodic orbits, basins of attractions, and time of attraction as a function of particle

diameter d (and thus $\tilde{\varepsilon}$). (a,d,g) show z-coordinate of the last crossing of trajectory with the x-z

Poincare plane as a function of release location; flat regions are basins of attraction for the 2

attactors. (b,e,h) show 20 trajectories in 3d released along a vertical line at $y = 0$, $x = 0.334$,

$0.05 < z < 0.95$; denser cores indicate attractors. (c,f,i) show crossing of the same select 20

trajectories with the x-z Poincare plane, color coded by time; blue corresponds to release

location, yellow corresponds to final positions.

1055
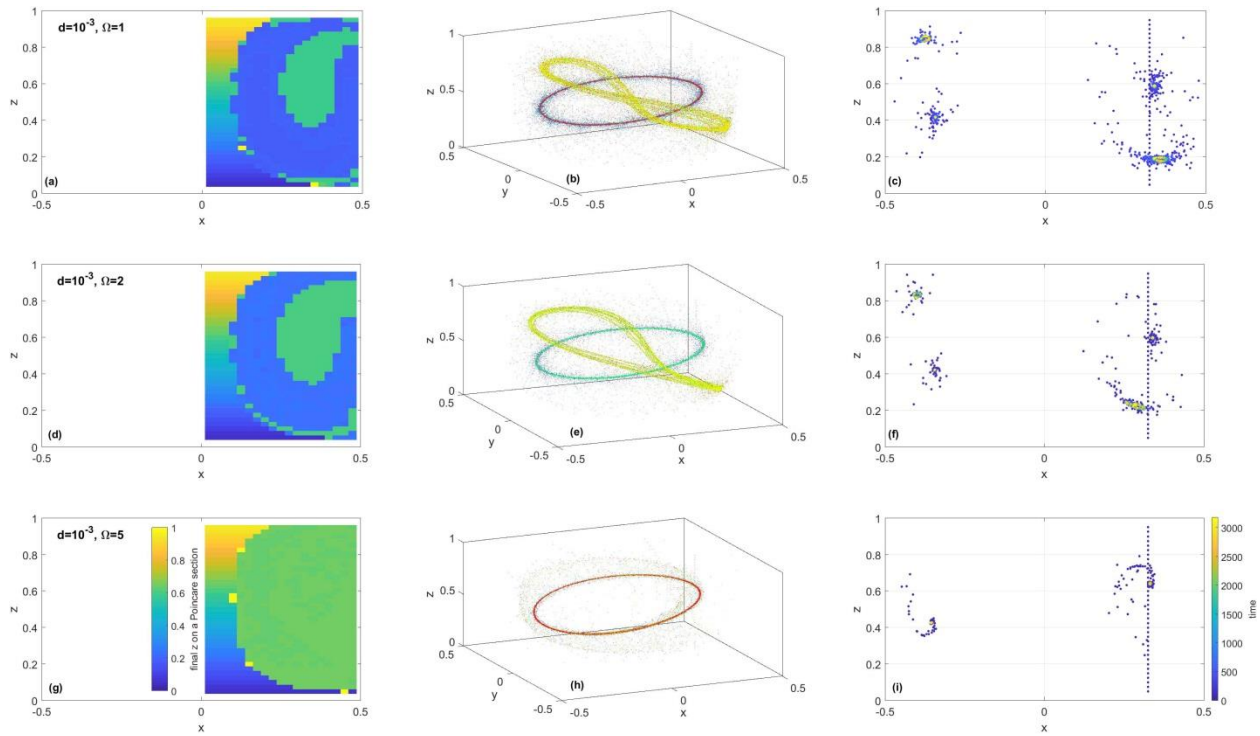
Figure 13. For the steady perturbed system (Experiment 2 in Table 1), changes in the location of the attracting periodic orbits, basins of attractions, and time of attraction as a function of frame rotation Ω. (a,d,g) show z-coordinate of the last crossing of trajectory with the x-z Poincare plane as a function of release location; flat regions are basins of attraction for the 2 attactors. (b,e,h) show 20 select trajectories in 3d released along a vertical line at $y = 0$, $x = 0.334$, $0.05 < z < 0.95$; denser cores indicate attractors. (c,f,i) show crossing of the same 20 trajectories with the x-z Poincare plane, color coded by time; blue corresponds to release location, yellow corresponds to final positions.